Solid-solution hardening by hydrogen in Fe-Cr-Ni-based austenitic steel: temperature and strain rate effects

Yuhei Ogawa[a], Osamu Takakuwa[b], Kaneaki Tsuzaki[a,c]

a *Research Center for Structural Materials, National Institute for Materials Science (NIMS), 1-2-1 Sengen, Tsukuba, 305-0047, Japan*
b *Department of Mechanical Engineering, Kyushu University, 744 Motooka, Nishi-ku, Fukuoka 819-0395, Japan*
c *Professor Emeritus, Kyushu University, 744 Motooka, Nishi-ku, Fukuoka 819-0395, Japan*

Corresponding Author: Yuhei Ogawa
E-mail: OGAWA.yuhei@nims.go.jp

Abstract

Solid-solution hardening caused by dissolved hydrogen (H) atoms in face-centered cubic metals is a favorable phenomenon that counteracts the H-induced degradation of mechanical performance in structural alloys, *i.e.*, hydrogen embrittlement. In the present study, the changes of yield and flow stresses by solute H with the concentrations of 2000~7600 at ppm were systematically investigated in a Fe-24Cr-19Ni-based austenitic stainless steel under the temperature range of 173~423 K and two different strain rates: 5×10^{-5} and 5×10^{-3}/s. Stress relaxation tests were subsidiarily employed in order to elaborate the underlying mechanisms predominating the H-related hardening at low and ambient temperatures. Four essential ingredients of the H-induced hardening were identified: (i) H atoms in the matrix lattice as dispersed obstacles; (ii) pinning of stationary dislocations by H atmosphere; (iii) dynamic pinning of dislocations resting at obstacles; (iv) drag force to moving dislocations by migratable H clouds. The hardening around 173 K was attributed to (i) and (ii), where the primary importance of interstitial-substitutional interaction between Cr and H was explicitly invoked. Meanwhile, the magnitude of hardening was maximized at around 298 K under the slow strain rate condition owing to the increasing contributions from (iii) and (iv).

Keywords: Austenitic stainless steel; Hydrogen; Solid-solution hardening; Dislocations

1. Introduction

In face-centered-cubic (FCC) metals and alloys, interstitial hydrogen (H) atoms are known to cause an intense augmentation of yield strength, flow stress, and indentation hardness [1–10]. The phenomenon was first elaborated in an old paper by Boniszewski and Smith in electrochemically charged pure Ni [1], later identified in Ni-based alloys [3,8,11,12], austenitic stainless steels (ASSs) [4–7,9], and FCC high-entropy alloys (HEAs) [13–15]. Despite its notable hardening effect, a significant drawback of the H occlusion has long been recognized: the ductility is degraded simultaneously, *i.e.*, hydrogen embrittlement, owing to the premature failure accompanying intergranular or cleavage-like fracture features [1,5,6,11–13,16]. Such a negative aspect still impregnates the well-accepted understanding of H as a detrimental element rather than a proactive agent for structural metals [17–19]. However, the present authors recently uncovered a concurrent improvement of the strength and ductility in ASSs with specific chemical compositions after uniformly charging an extensive amount of solute H (~7000 at. ppm) [20,21]. This epoch-making finding now gives rise to a prospect for utilizing H to strengthen the ASSs in the same manner as other interstitials like carbon (C) and nitrogen (N) [22–26].

The hardening by interstitial atoms is generally attributed to the statistical interactions between dislocations and short-range lattice strain or different modulus zone around the interstitials: solid-solution hardening [27–31]. Nevertheless, because of its small atomic diameter and extensive diffusivity, several forms of dynamic interactions of diffusible H and mobile dislocations have been of great importance in understanding the rationales behind the H-induced strengthening effect [1,3,4,8,32–36]. Such dynamic interactions were evidenced by serrated yielding in H-charged Ni and Ni-alloys within the temperature and strain rate ranges in which the diffusion of H and the velocity of dislocations become mutually competitive [1–3,37,38]. Segregation of H into dislocation core region and potential nucleation of local hydride phase [2,4,39–41] pin the mobile dislocations, leading to the intermittent stress drop (*i.e.*, Portevin-Le Chatelier effect) in association with the dislocations depinning or activation of other dislocation sources. The latter event results from the exhaustion of mobile dislocations due to the dynamic pinning, which amplifies dislocation density and substructure evolution, thereby enhancing the work-hardening as a secondary impact [37]. H-induced dislocations pinning was further supported in Ni-Cr alloys by identifying the yield point discontinuity after static strain-aging experiments [42]. Moreover, the hardening outcome has also been ascribed to the changes in dislocation gliding character when the dislocation velocity is slow enough to allow the coordinative motion of its segregated H atmosphere [8,16,34,43]: planar dislocation structures or smaller cell sizes are favored owing to a suppressed cross-slip [9,44,45] and shielding of the elastic stress field around dislocations, *i.e.*, H-enhanced localized plasticity (HELP) theory [32,46].

On the other hand, in Fe-Cr-Ni-based ASSs and HEAs, critical information is lacking for getting to the bottoms of H-induced strengthening phenomena [4,6,7,9,15,20,35]. Despite their coordinative capability for the hardening with Ni and Ni-alloys [1,3,8,11], it is still not explicit whether the responsible H-dislocation interactions are dynamic, static, or both. A careful examination of the tensile flow behavior was conducted by Altstetter and co-workers on the thin foils of AISI Type304 and 310S steels after cathodically charging ~10 at% H [4–6]. They found that the escalation of yield stress by solute H in austenite was comparable to those caused by C and N, which was later reproduced in the bulk samples of ASSs thermally charged in a pressurized H_2 gas environment [21]. Upon the H concentration exceeding 5 at%, a distinct yield drop appeared on the stress-strain curve, attributed to the locking of pre-existing dislocations and dislocation sources by forming the H-Cottrell atmosphere [4–6]. However, the re-appearance of such yield drop or its amplification by H was not confirmed when the materials were pre-strained, aged, and re-strained at room temperature [5,20]. This implies that the pinning effect of dislocations by H at ambient conditions is, if any, not so significant or might be weaker than that in Ni alloys. A strain localization due to HELP (*i.e.*, reduction in the effective gauge length) was also pointed out as a trigger of the apparent hardening effect [9,32,36]. Although, the strengthening that emerged at cryogenic temperature or high strain rate [12,15,20,47], where coordinative H-dislocation motion is infeasible, contradicts the presumptions in the HELP hypothesis [32,46].

In terms of the static solute-dislocation interactions, the presence of H-H or substitutional-H pairs, which may function as short-range and thermally-activatable obstacles *via* lattice swelling or tetragonal distortion, was implicated in the internal friction measurements [48–50]. Indeed, Koyama et al. recently identified that an H-charged HEA contained an enhanced thermal component in its yield stress [15]. Moreover, through a continuum mechanics study of the dynamic interactions between diffusible interstitials and perfect/extended dislocations, a significant contribution of the H-atmosphere dragging to obstructing dislocation movement was simulated by Sills and co-workers [35,51]. In the course of practical tensile deformation, either or several of these factors and possibly some different ones may selectively or synergistically be activated, predominating the H-induced strengthening as a final consequence. Ultimately, a more systematic experimental framework is now required to isolate the leading mechanisms under given deformation conditions.

The most elemental approach to probe the solute-dislocation interactions is to examine temperature- and strain rate-dependences as well as thermal activation behaviors of plastic flow [15,23,52–58]. In the present study, a Fe-24Cr-19Ni-based (AISI Type310S) ASS was uniformly charged with 2000~7600 at ppm solute H. Yield/flow stresses, work-hardening characteristics, stress-relaxation properties, and strain rate-sensitivity were evaluated under a wide range of temperature. The rationales of the solution hardening were classified into several essential ingredients incorporating both the static and dynamic effects. Finally, individual contributions from these controlling factors were weighted as a function of the employed experimental variables.

2. Material and experimental methods

The materials used in this study was a commercially available Type310S ASS with a chemical composition shown in Table 1. A hot-rolled bar with a diameter of 20 mm was solution-annealed at 1353 K, followed by water-quenching, resulting in a grain size of 40~70 μm (see Fig. 1 (a)). The cylindrical tensile specimen having a 6 mm diameter and 30 mm-interval flanges on its gauge part (Fig. 1 (b)) was machined, the surface of which was finished by polishing with #1000 silicone-carbide paper.

Tensile tests were performed with a screw-driven electromechanical test frame attached to a thermostat chamber. The tests were conducted at temperatures of 173~423 K with crosshead displacement speeds (CHS) of 0.0015 and 0.15 mm/s, corresponding to the initial strain rates of $\approx 5\times10^{-5}$ and 5×10^{-3}/s, respectively. The elongation of the gauge part between the two flanges was monitored by using a linear variable differential transformer (LVDT). Additionally, stress-relaxation tests were carried out at 173 and 298 K with the same testing equipment. The crosshead position was fixed after applying the true strain of 0.06 with CHS = 0.0015 mm/s, and the stress decay was recorded as a function of time for 500 s with a data acquisition interval of 0.2 s.

Some of the tensile specimens were H-charged by exposing them to a pressurized gaseous H_2 environment at 543 K for 200 hours in an autoclave. Considering the H diffusion coefficient in Type310S ASS, the charging temperature and duration are enough to realize a uniform distribution of solute H inside the gauge part of the tensile specimen with a 6 mm diameter (see authors' previous publications [20,21] for detail). For varying the H concentration, the H_2 gas pressures for charging were set as 10, 40, 70, and 100 MPa. We also checked that the heating at elevated temperature itself and possible microstructural changes do not affect the mechanical behavior by preparing a specimen that was heat treated in a vacuum at 543 K and 200 hours.

After the tensile tests, cylindrical samples with a height of 5 mm were cut from the uniformly deformed parts of the specimens, the residual H concentrations of which were measured by gas chromatography thermal desorption analysis (TDA). The temperature range and heating rate for the TDA were 298~1073 K and 100 K/h, respectively.

Table 1 Chemical composition (mass %) of Type 310S stainless steel used in this study.

C	Si	Mn	P	S	Ni	Cr	Fe
0.02	0.37	1.10	0.023	0.001	19.18	24.18	Bal.

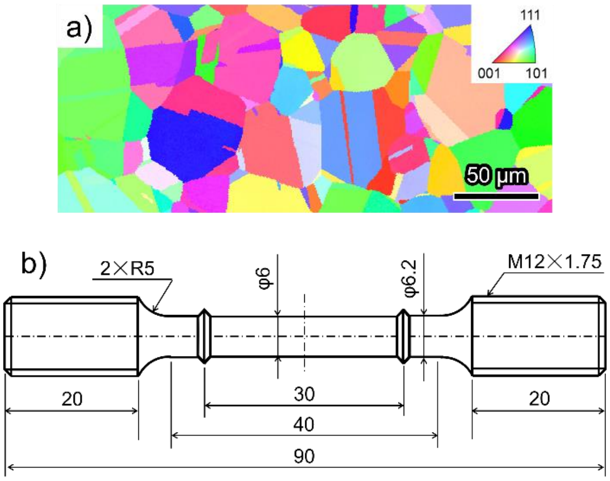

Fig. 1 (a) Initial microstructure on the plane perpendicular to the bar-axis, analyzed by electron backscattering diffraction. (b) dimensions (mm) of the tensile specimen.

3. Results

3.1 Hydrogen absorption property

The dissolution behavior of H atoms into the crystal lattice of metals from a gaseous phase follows Sievert's law [59], wherein the saturated solute H concentration, C_0, is correlated with the solubility, K_S, as follows.

$$C_0 = K_S\sqrt{f} \tag{1}$$

Here, f is the fugacity of H_2 gas, which is defined by the Abel-Noble equation of state,

$$f = P\exp\left(\frac{Pb_0}{RT}\right) \tag{2}$$

where P is H_2 gas pressure, b_0 = 15.84 cm^3/mol [59], R is the universal gas constant, and T is the absolute temperature.

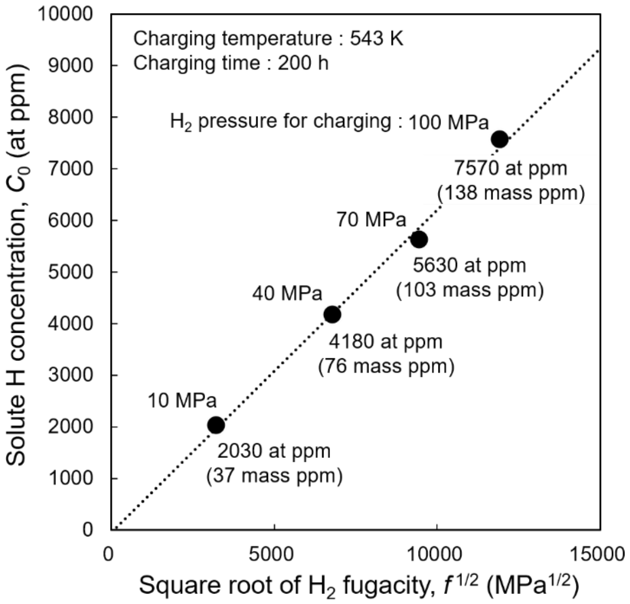

Fig. 2 Solute H concentration as a function of the square root of H_2 gas fugacity for charging. The linear relationship indicates the satisfaction of Sievert's law.

In Fig. 2, the H concentrations in the specimens in this study are plotted versus the square root of H_2 fugacity corresponding to the charging temperature and pressure conditions in line with eq. (1). A linear relation was obtained between the two parameters with K_S = 0.62 at ppm/MPa$^{1/2}$, indicating that the solute H atoms primarily dissolved into interstitial lattice sites (*i.e.*, octahedral sites in FCC crystal) rather than defects, such as grain boundaries and pre-existing dislocations. The maximum H concentration of 7570 at ppm (138 mass ppm) was achieved after charging at 100 MPa, consistent with the authors' previous research using a same-grade material [20,21]. The measurement error of the H concentration under each charging condition was within ±5% and even reduced to ±2% as the charging pressure increased from 10 to 100 MPa. Note that in the fractured specimens tested at 373~423 K, a ~10% decrease of the residual H concentration was recognized due to an enhanced H diffusion. Nevertheless, the influence of H-loss on the mechanical properties could be trivial because the H desorption should be limited at the near-surface parts as well as because the focus of this paper was a small strain domain after yielding where the test duration was much shorter than that until the fracture.

3.2 Tensile flow behavior

3.2.1 Effect of deformation temperature

Fig. 3 depicts the true stress-true strain curves of the small strain domain covering the yield point of non-charged and H-charged specimens with C_0 = 7570 at ppm at five different deformation temperatures (*i.e.*, 173, 223, 298, 373, and 423 K). In what follows, the standard CHS for acquiring the presented results is 0.0015 mm/s (*i.e.*, initial strain rate of 5×10^{-5}/s) unless otherwise noted. Comparing the solid and open symbols at each temperature, one can notice that evident escalations of the yield and flow stresses emerged owing to the H-charging at temperatures below 373 K, while the effect was gradually diminished as the temperature increased.

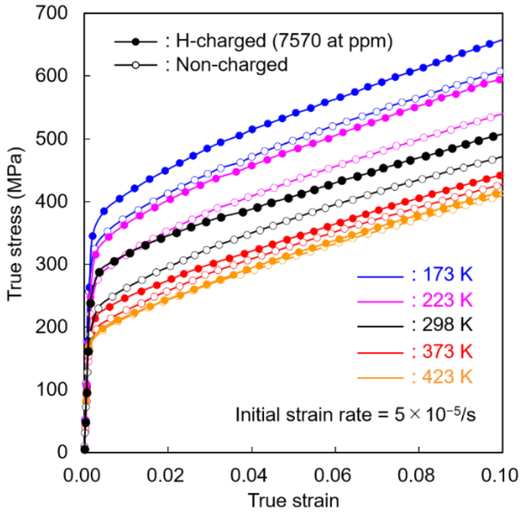

Fig. 3 True stress-true strain curves of non-charged and H-charged (C_0 = 7570 at ppm) specimens for the strain range of ~0.10 at five different deformation temperatures.

The yield stresses (0.2% proof stresses, $\sigma_{0.2}$, defined on the true stress-true strain curves) were extracted from Fig. 3, and their absolute values, as well as the gaps between non-charged and H-charged specimens (*i.e.*, the magnitude of solid-solution hardening at yielding), are plotted as a function of deformation temperature in Fig. 4 (a) and (b). Monotonic increases of the yield stress with the decrease in temperature were apparent both in non-charged and H-charged specimens, whereas the magnitude of H-induced strengthening was maximized at 298 K. At the lower temperatures, the strengthening was still substantial, yet the extent was smaller with respect to that at 298 K.

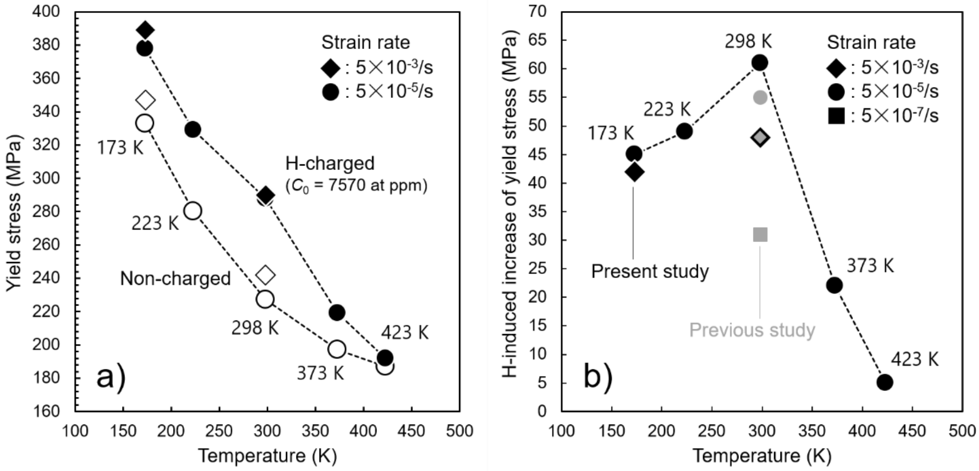

Fig. 4 (a) yield stress (0.2% proof stress) in non-charged and H-charged (C_0 = 7570 at ppm) specimens and (b) their gaps at five different deformation temperatures under several strain rate conditions. The authors' previous data on Type310S steel with similar hydrogen concentration [20] are plotted as three gray marks in (b) for comparison.

Fig. 5 (a)~(e) show the work-hardening rate curves of the non-charged and H-charged (C_0 = 7570 at ppm) specimens at five testing temperatures plotted against true stress. The stress of each specimen was presented after subtracting the yield stress from the total flow stress for canceling the contribution of solid-solution hardening on the horizontal axis. Also, both axes were normalized by shear modulus, *G*, at each temperature [60] in order to eliminate the modulus-dependent component of the work-hardening rate and flow stress [61]. Interestingly, the work-hardening rate in the H-charged specimen at 298 K exhibited a temporal decay after yielding, recovering gradually and then merging into the curve of the non-charged specimen with the increase of stress and strain (Fig. 5 (c)). The same phenomenon was discovered in our previous publication [21], yet the underlying reason was ambiguous. However, such a transient work-hardening behavior in the H-charged specimen notably disappeared when the temperature was both increased and decreased from 298 K: the curves of non-charged and H-charged specimens became coincident with each other.

In Fig. 5 (f), the gaps in flow stress between non-charged and H-charged specimens at each temperature are indicated as a function of true strain, wherein the underlying reason for the temporal decay of work-hardening at 298 K (Fig. 5 (c)) is now uncovered. That is, even though the flow stress gap at 298 K was the greatest among the five temperatures at the beginning of deformation, it suddenly decreased by almost 30 MPa as the strain evolved to 0.05, then settled with the value falling below those at 223 and 173 K. A similar but a weaker strain-dependent tendency of the flow stress gap was observed at 373 K. Meanwhile, at other three temperatures, the gap of flow stress remained almost constant irrespective of strain within a range of fluctuation, except for a sudden decrease immediately after the onset of yielding at 173 K.

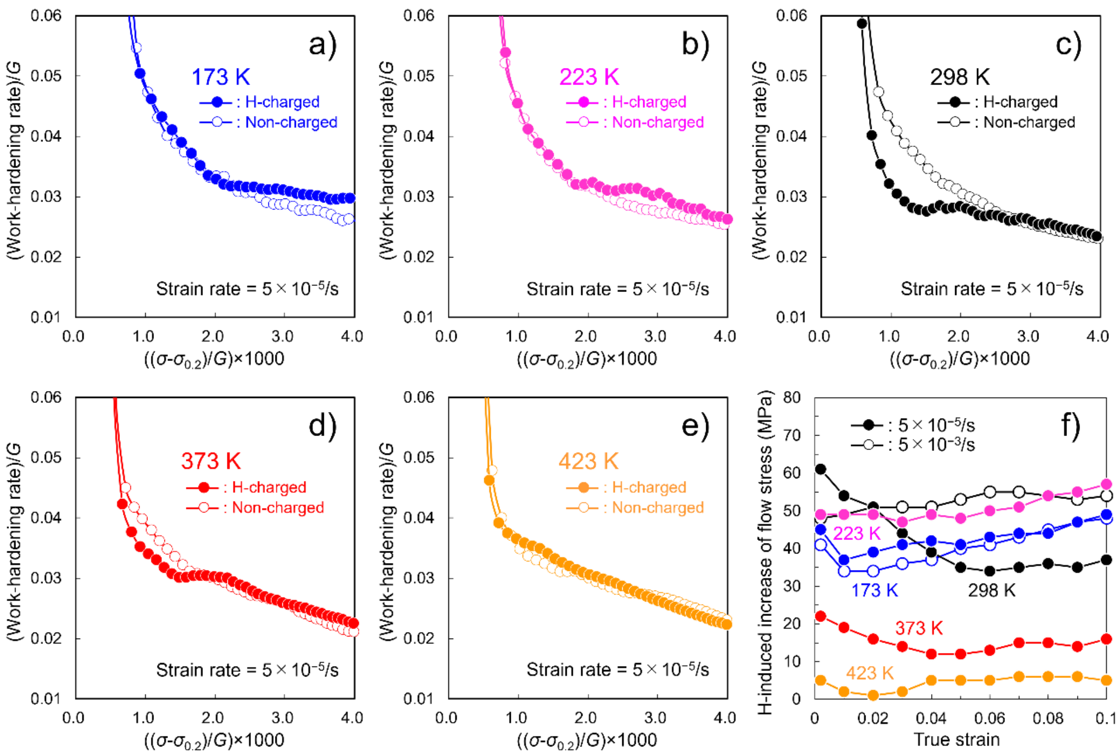

Fig. 5 (a)~(e) work-hardening rate versus flow stress curves of non-charged and H-charged (C_0 = 7570 at ppm) specimens at 173~423 K and a strain rate of 5×10^{-5}/s, wherein the vertical and horizontal axes were normalized by shear modulus at each temperature. (f) depicts the gap of flow stress between non-charged and H-charged specimens at 173~423 K and at two different strain rates as a function of true strain.

3.2.2 Effect of strain rate

The influence of strain rate was examined at two representative temperatures of 298 and 173 K. Two orders of magnitude faster CHS than the standard one (*i.e.*, initial strain rate of 5×10^{-3}/s) was applied for non-charged and H-charged (C_0 = 7570 at ppm) specimens. The yield stress, as well as its magnitude of enhancement by H, are inserted in Fig. 4. In the non-charged specimens, the faster strain rate resulted in slightly higher yield stress at both testing temperatures, as supposed from the basic thermal activation theory of dislocation dynamics [62]. The yield stress of the H-charged specimen was also augmented at 173 K (Fig. 4 (a)), although the magnitude of yield stress enhancement by solute H was rather independent of strain rate (Fig. 4 (b)). Notwithstanding, the most notable discovery here was that no recognizable impact of strain rate manifested on the yield stress of the H-charged specimen at 298 K (Fig. 4 (a)). According to the strain rate-dependent increase of yield stress in the non-charged specimen at 298 K, this led to a weakened solid-solution hardening by H, as is visible in Fig. 4 (b).

In order to check the reproducibility of the experimental results, Fig. 4 (b) also includes the yield stress enhancement under three different strain rates (5×10^{-3}, 5×10^{-5}, and 5×10^{-7}/s) at 298 K measured in our previous paper on the same grade material with identical solute H concentration [20]. An agreement between the previous and present results was confirmed at the strain rates of 5×10^{-3} and 5×10^{-5}/s. Furthermore, the yield stress enhancement by H at 5×10^{-7}/s was smaller than those at 5×10^{-3} and 5×10^{-5}/s: the strain rate dependence of the solid-solution hardening at the yield point in the H-charged samples was not monotonous.

The flow stress gaps between non-charged and H-charged specimens under a faster strain rate of 5×10^{-3}/s are overlaid in Fig. 5 (f). It is noteworthy that the overall flow stress augmentation by H was more remarkable, and no stress drop was seen under the faster strain rate at 298 K, while the yield stress increase was inferior to that at the slower strain rate (Fig. 4 (b)). In contrast, the magnitude and propensity of the increase in flow stress were almost independent of the strain rate at 173 K.

3.2.3 Effect of H concentration

At 298 and 173 K, where H-induced strengthening was substantial, the H concentration dependence of the flow behavior was also studied. The true stress-true strain curves around the yield point and small strain domain are shown in Fig. 6 (a). The yield stresses were augmented as a monotonic function of C_0 at both temperatures, although temporal decreases of the flow stress below those of non-charged specimens were observable after yielding, particularly at low H concentrations, as clearly seen in Fig. 6 (b) and (c).

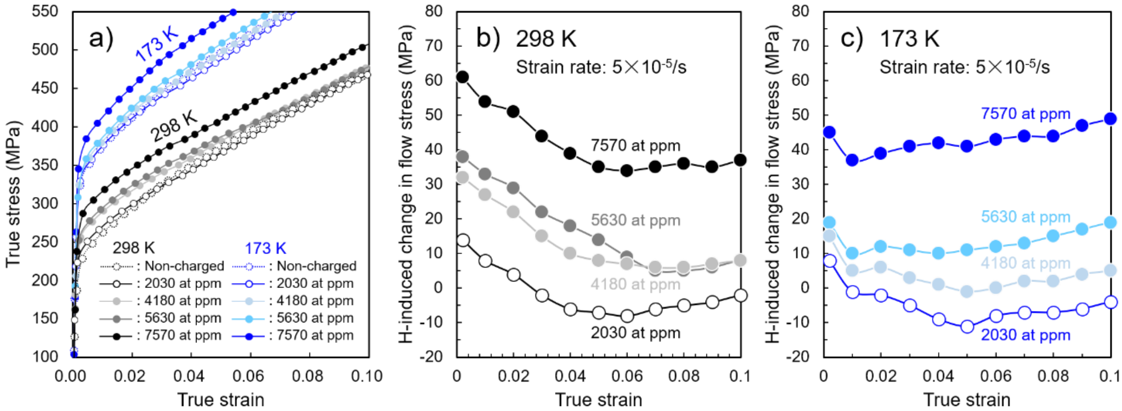

Fig. 6 (a) true stress-true strain curves of the non-charged specimen as well as the H-charged specimen with various H concentrations at 298 and 173 K with the strain rate of 5×10^{-5}/s. (b) and (c) show the gap of flow stress between the non-charged and H-charged conditions, which were derived from (a).

Fig. 7 (a) and (b) present the H concentration-dependence of the magnitude of yield stress enhancement at 298 and 173 K. The increase in yield stress was linearly correlated with the solute H concentration with the slope of $\approx G/86$ at 298 K, a result that coincides with the tendency acquired in the authors' previous study on some ASSs with various Cr and Ni contents [21] as overlayed in Fig. 7 (a). On the other hand, a non-linear interrelation between the H concentration and the yield stress increase was recognized at 173 K (Fig. 7 (b)). Rather, the yield stress was amplified in a slightly exponential tendency with augmenting the H concentration.

The gaps between the flow stress in the non-charged specimen, as well as H-charged specimens with different H concentrations, are depicted in Fig. 6 (b) and (c), like Fig. 5 (f). At 298 K, the shape of the four curves was not significantly changed by the H concentration, and the overall curve shifted downward with the decrease of C_0. However, the propensity at 173 K was somewhat different from the case of 298 K. Namely, the gradual decay of the flow stress gap toward 0.05 true strain, which was milder but reminiscent of the behavior at 298 K, emerged at lower H concentrations of 2030 and

4180 at ppm, although such temporal decay was not distinct at 7570 at ppm H. Additionally, a sudden drop of the stress gap between the yield point and 0.01 true strain was a common distinction under all the examined hydrogen concentrations.

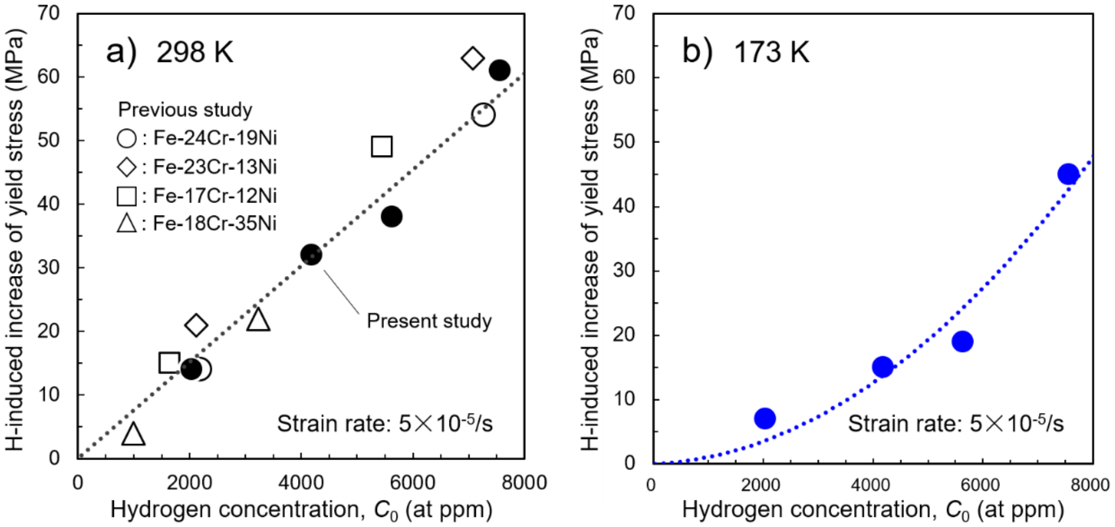

Fig. 7 Increases of the yield stress (0.2% proof stress) by H-charging, which were measured at 298 and 173 K with a strain rate of 5×10^{-5}/s, as a function of linear H concentration. The results of some ASSs with different Cr and Ni contents measured in the authors' previous study [21] are plotted together with open symbols in (a).

3.3 Stress relaxation behavior

Fig. 8 (a) shows the stress-relaxation curves of non-charged and H-charged specimens (C_0 = 7570 at ppm) at 298 and 173 K, where the stress at the beginning of relaxation for each specimen is defined as zero. Note that the fluctuation on the curves in 173 K is not a specific material behavior but merely a noise associated with the data recording at a cryogenic temperature. For both temperatures, large relaxation occurred during the first 100 s, followed by gradual settling down of the stress decay in the remaining time frame. The amount of relaxation was larger in the H-charged specimens, yet the temperature dependence was distinct depending on the presence and absence of H. In the non-charged specimens, more rapid relaxation ensued in a shorter time at 173 K, eventually ceasing upon the passage of 500 s. On the other hand, the relaxation rate at 173 K was slower than that at 298 K in the H-charged specimens, a totally different tendency from the non-charged case. The distinct stress relaxation behavior between non-charged and H-charged specimens was also apparent when focusing on the short time period, as depicted in the inset of Fig. 8 (a). Namely, during the first 20 s, H-charging resulted in an obviously accelerated relaxation rate at 298 K, while the relaxation curves of non-charged and H-charged specimens were close to each other at 173 K. As the relaxation time exceeded 10^2 s, the two curves at 173 K eventually diverged.

In Fig. 8 (b), the stress-relaxation results are reproduced in the form of the absolute stress values versus the logarithm of the relaxation time. Under all the experimental conditions, the curves were almost straight after 10 s relaxation, indicating a typical logarithmic transient observed in most metallic materials [58]. The slope of the logarithmic relaxation curve of the H-charged specimen was steeper than that in the non-charged one at 298 K, merging into each other as the curves were extrapolated to the relaxation time of 10^7 s order. Meanwhile, the curves of H-charged and non-charged specimens were mutually more parallel at 173 K, which implies that a much longer time would be required for the two curves to be finally merged.

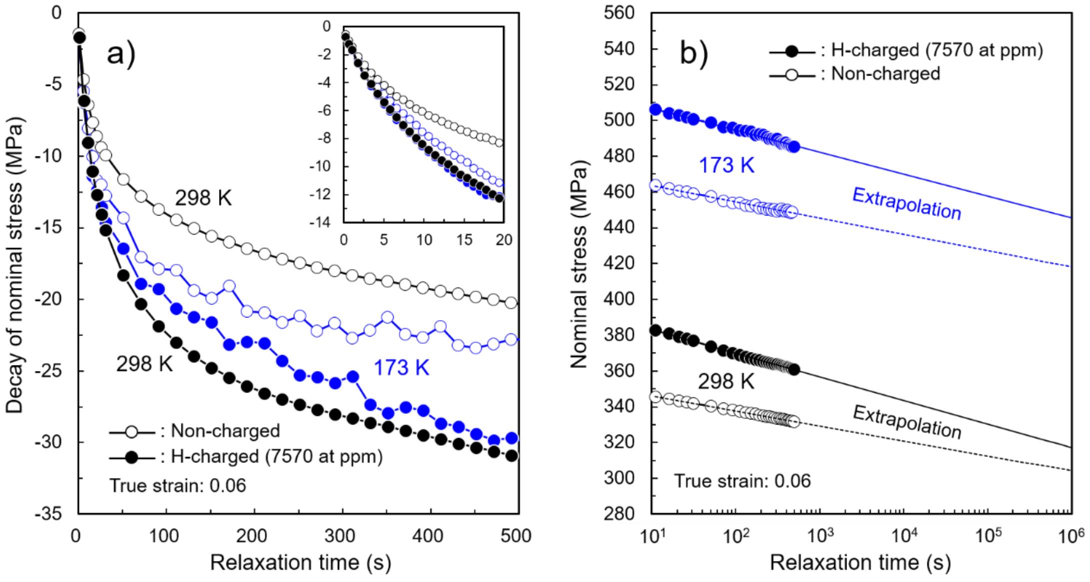

Fig. 8 Stress relaxation curves of non-charged and H-charged (C_0 = 7570 at ppm) specimens at 298 and 173 K after applying a true strain of 0.06 with a strain rate of 5×10^{-5}/s. The relaxation time in the horizontal axis is linear in (a), while it is logarithmic and extrapolated into longer time scales in (b). The inset in (a) magnifies the relaxation curves at the beginning short time period.

4. Discussion

4.1 Preface

The hardening of FCC metals and alloys *via* H occlusion has often been discussed from the perspective of the H-induced plasticity localization (*i.e.*, HELP) model [5,6,9,32,36,63]. Suppression of dislocations cross-slip may decrease the number of active slip planes, rendering the distribution of slip bands coarser and more heterogeneous [5,6,9]. As a result, the effective gauge length bearing the applied strain is reduced, as well as the density of mobile dislocations in individual slip bands is augmented [32,36]. These scenarios bring about an escalated flow stress under a given macroscopic strain. An alteration in the deformation mode caused by H also affects the evolution of dislocation substructures and resultant work-hardening [8,16,34,43]. In conform to the HELP model, H atoms segregating around a moving dislocation shield its elastic stress field in addition to inhibiting cross-slip [32,44,46,64]. Such modifications potentially shrink the dislocation cell size or promote the formation of more planar dislocation substructures [16,34,43], playing a role in amplifying the flow stress as a secondary influence.

In ASSs, the modification of dislocation behavior, particularly slip localization, has been evidenced by the increases in slip line spacing and height on the material surface [5,6,65]. Nonetheless, Aubert et al. statistically analyzed the slip line distribution of a Type316L steel with grain sizes of 140 and 300 μm charged with ~135 mass ppm H [63]. They identified that the H-impact on the strain localization was minor for the material with a smaller grain size, especially under a small strain regime with a few percent. Kamei et al. reported the results of dislocation density measurement *via* X-ray on a 316L steel, wherein the difference between non-charged and H-charged samples was not significant until the strain reached ~20% [66]. Even in the authors' experiments, no H-effect was recognized in the work-hardening rate, except for the peculiar domain immediately after yielding at ambient temperature (Fig. 5) and a large strain regime where deformation twinning commenced [20,21,67]. Kocks and Mecking, who elaborated on the work-hardening in FCC metals, pointed out that the dislocation structures (*i.e.*, density and arrangement) exhibit a mutually similar distinction when a given material undergoes an identical work-hardening rate [61]. Taking these perceptions, the grain size (*i.e.*, 30~70 μm), and the targeted strain level in the present study into account, the H-induced hardening in ASSs is not merely an indirect consequence of the strain localization and the modification of dislocation glide/accumulation characteristics. Rather, a major part of the hardening should rely on the intrinsic effects of H, which act as obstacles to the movement of individual dislocations. The manifestation of stress enhancement at 173 K (Fig. 3), where the formation of an H-dislocation atmosphere during deformation would be infeasible, also supports such a presumption. Note that when discussing H-material interactions, H segregation and diffusion along grain boundaries are sometimes of great importance [12,18,68]. Even concerning the yield strength, the segregation of interstitial atoms (*e.g.*, C and N) along grain boundaries possibly affects the mechanical behavior *by* altering the extent of the Hall-Petch strengthening [69]. However, it has been clarified in Type310S ASS that the trapping is negligible due to almost equivalent solution energy of H between grain boundaries and interstitial lattice sites [70]. Thus, we assume that the grain boundary effect on the yield stress change after H-charging is trivial, and the interactions of H with dislocations are much more critical.

The glide resistances arising from solutes are classified into lattice friction by dispersed atoms [27,31], pinning by Cottrell atmosphere around a stationary dislocation [29,71], a force pulling back the dislocation *via* solute drag [35,72], and dynamic pinning (*i.e.*, dynamic strain-aging, DSA) [56,73,74]. In the following sub-sections, contributions from these multiple factors at each temperature are discussed based on the findings provided in Section 3. Note, on the other hand, that enhanced mobility of dislocations by H has, contrary, been envisaged through an accelerated velocity of dislocations in *in-situ* transmission electron microscopy (TEM) studies [32,46,64,75]. Nevertheless, recent molecular dynamics simulations revealed that solute H indeed obstructs the dislocation movement except for some specific cases [33,76,77], arguing that what was observed in TEM was a unique phenomenon that occurs only in thin foils [78].

4.2 Mobility of H atoms during deformation

In an attempt to evaluate the significance of the above-listed roles of solutes that resist dislocation movement, an estimation of H mobility during deformation is a principal piece. Several researchers experimentally measured the H diffusivity in 310S steel by means of gas desorption or permeation techniques [79–82], in which the temperature dependence of the diffusion coefficient, D, followed the Arrhenius equation:

$$D = D_0 \exp\left(-\frac{E_D}{RT}\right) \tag{3}$$

where D_0 is the pre-exponential factor, and E_D is the activation energy for lattice diffusion. Fig. 9 (a) shows the D vs. temperature curves obtained by plugging the D_0 and E_D values in the references [79–82] into eq. (3). The solid lines indicate the temperature ranges where diffusion data were experimentally acquired in [79–82]. Since the measurement of diffusivity in ASSs at lower temperatures is infeasible, we were compelled to extrapolate these data owing to eq. (3), as described by dashed lines in Fig. 9 (a). Once the plastic deformation commences, the bulk hydrogen diffusivity is more or less affected by the defect-trapping effects, particularly when the temperature is low [18,79,83]. Nevertheless, extrapolation of eq. (3) can be a good approximation in the present case because it is the lattice diffusivity that predominates the interactions between diffusible solutes and mobile dislocations [51,56,72].

Considering a random jump of an H atom from an octahedral (O-) site to the neighboring twelve O-sites, the diffusivity data also gives an estimation of the jump frequency of H, f, through the lattice parameter, a (approximated as 3.6 nm), as $f = 12D/a^2$. The f vs. temperature curves derived from Fig. 9 (a) are reproduced in Fig. 9 (b). At 173 K, the f lies at 10^{-5}~10^{-2}/s. The time for acquiring the data in Fig. 3 and Fig. 6 was the order of 10^3 s, denoting that H barely migrated through the lattice at such a low temperature. Meanwhile, H becomes substantially active at 298 K, with the f beyond 10^4/s. Therefore, some forms of dynamic interactions with mobile dislocations are anticipated at and above 298 K.

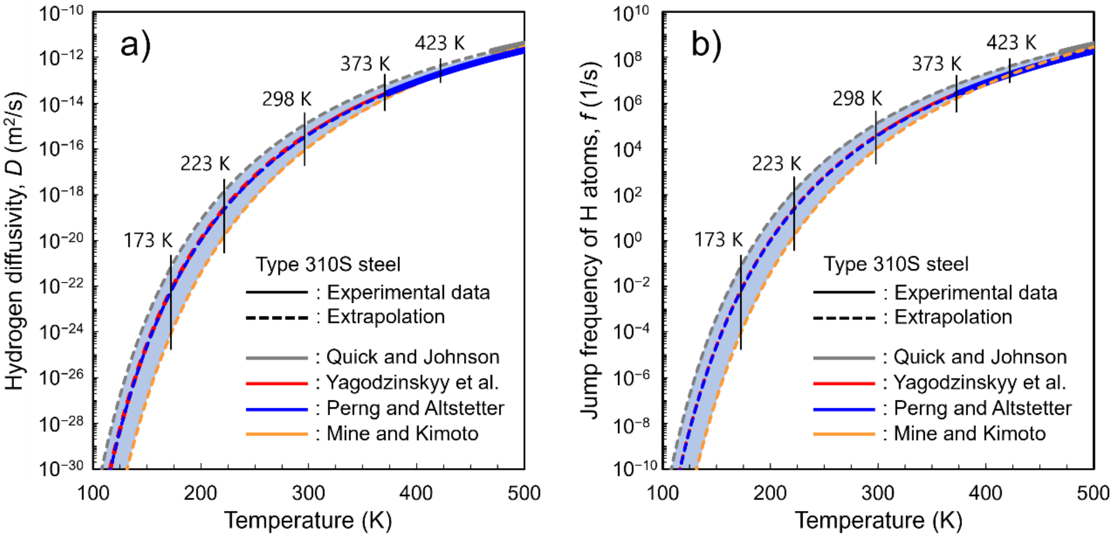

Fig. 9 Diffusion coefficient (a) and jump frequency (b) of H atoms in Type310S steel, which were previously measured by several researchers [79–82]. The solid lines denote the experimentally acquired data, while the dashed lines are the extrapolation of the experimental data *via* eq. (3).

4.3 Estimating H segregation around a dislocation

The strength of the interaction between H and a stationary dislocation [4,40–42,77] is another essential factor for scrutinizing the H-induced hardening. In this sub-section, the segregation of H around a perfect edge dislocation was examined by simply assuming the size effect driven from the stress field around the dislocation line (*i.e.*, Cottrell atmosphere [29,71]). Even though the presumption fails to assess the segregation to the core where linear elasticity breaks down [29,71] and neglects any electronic effects [39,40,84], it still provides qualitative information regarding the magnitude of H-dislocation interactions at each temperature. Additionally, since the dislocations in FCC metals with low to medium stacking fault energy (*e.g.*, ≈ 40 mJ/m^2 in 310S steel [85]) are extended into two Shockley partials, the H segregation into screw dislocations through the size effect is also plausible [29,51].

In a solid-solution with an average solute concentration of C_0, the local concentration around a segregation (trapping) site, C_T, obeys the Fermi-Dirac formula.

$$\frac{C_\mathrm{T}}{1-C_\mathrm{T}} = \frac{C_0}{1-C_0}\exp\left(\frac{E_\mathrm{B}}{RT}\right) \tag{4}$$

Here, E_B is the binding energy of the trap site with a solute atom. Assuming a positive edge dislocation lying along the *z*-axis in a Cartesian coordinate, the distribution of E_B due to the dislocation's dilatational stress field on the *x*-*y* plane is given as [29]:

$$E_B = \beta\frac{y}{x^2+y^2} \tag{5}$$

$$\beta = \Delta V\frac{Gb}{3\pi}\left(\frac{1+\nu}{1-\nu}\right) \tag{6}$$

where b is the Burgers vector (≈ 2.5×10^{-10} m), ν is Poisson's ratio, and ΔV is the swelling volume per solute atom for which ≈ 2×10^{-30} m^3 were experimentally and analytically reported in the case of H [86,87]. β is called an elastic interaction parameter.

Fig. 10 (a)~(c) show the C_T distribution at the solute-condensed region below the slip plane, wherein $C_0 = 7570$ at ppm and three different temperature conditions were adopted. In ASSs, E_B ≈ 13 kJ/mol was reported as the binding energy of H with dislocations [79,87–90], which is quite identical to the values in pure FCC metals such as Ni and Al [40,41,91]. The black dashed lines in Fig. 10 (a)~(c) delineate the border that corresponds to E_B ≈ 13 kJ/mol according to eq. (5). Although linear elasticity leaves some uncertainties in the proximity of the dislocation line, the results demonstrate that the E_B reported in the previous investigations [79,87–90] potentially reflects the H trapping at the dislocation core. The H segregation *via* the size effect spreads well outside the core, an extension of which enlarges with a decrease in temperature.

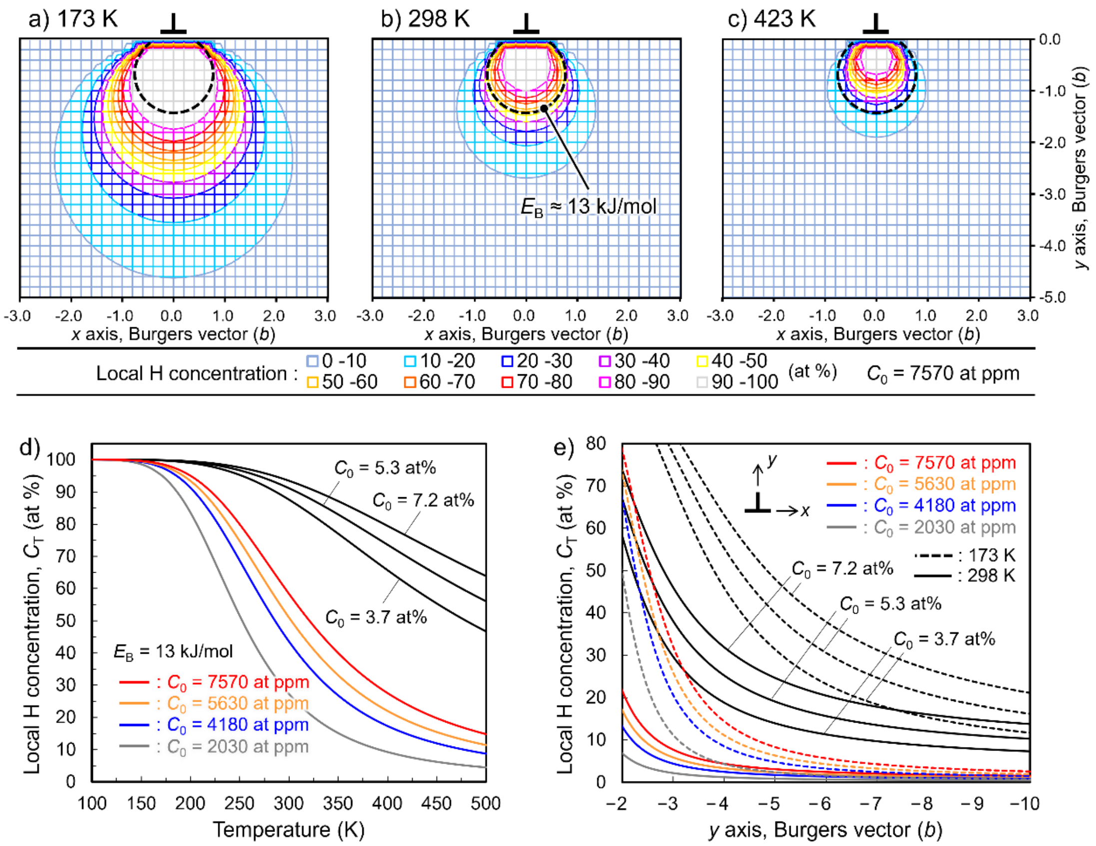

Fig. 10 Segregation behavior of hydrogen atoms around a perfect edge dislocation *via* size effect: (a)(b)(c) distribution of the Cottrell atmosphere at 173, 298, and 423 K under an average hydrogen concentration of 7570 at ppm; (d) temperature dependence of the local hydrogen concentration at dislocation core with E_B = 13 kJ/mol; (e) extension of the Cottrell atmosphere below the slip plane at 173 and 298 K under various average concentration of hydrogen. Note that the curves of Co of 3.7, 5.3, and 7.2 at % will be described and discussed in Section 4.7 later.

Fig. 10 (d) shows the temperature dependence of C_T, which was calculated according to eq. (4), at the region corresponding to E_B = 13 kJ/mol under various conditions of C_0. Above 200 K, C_T continuously increases with a decrease in temperature and depends significantly on C_0. Meanwhile, although the values close to 100% are physically unrealistic for interstitial solutes, it is apparent that the C_T at the dislocation core tends to saturate irrespective of C_0 at temperatures below 200 K. Note, however, that the situation is different outside the saturated core, as the C_T distribution along the negative side of the

y-axis is shown in Fig. 10 (e). In the regime away from the dislocation center, the H segregation depends on C_0 even at 173 K, in which the extent of the atmosphere becomes greater as C_0 increases. The same tendency can be seen at 298 K, while the overall H concentration in the atmosphere is low compared with 173 K.

At 173 K where H diffusion is slow, a completely equilibrated atmosphere (Fig. 10) was unlikely to be achieved. Even so, it took one hour to decrease the temperature to 173 K, and 10 minutes of preservation was interpolated before the start of the test: H atoms were allowed to migrate slowly through the lattice. According to an old treatment by Harper, the fractional interstitial segregation rate at a site with E_B is approximated as [92]:

$$q = 1 - \exp\left\{-2\rho\left(\frac{\pi}{2}\right)^{1/3}(E_B Dt/RT)^{2/3}\right\} \tag{7}$$

where ρ is dislocation density, and t is aging time. Taking $E_B \approx 4$ kJ/mol as a binding energy at the outer periphery of the Cottrell atmosphere (eq. (5)) and $\rho = 10^{12}$ m^2/m^3, q exceeds 90% after the passage of 4000 s at 173 K. Thus, the atmosphere should become wider and denser as the temperature is lowered, and it could take a quasi-equilibrated state close to the distribution shown in Fig. 10.

4.4 Contribution of solute drag

From the jump frequency estimation in Section 4.2, an emergence of dynamic H-dislocation interactions during deformation has been envisaged at and above 298 K. In fact, the magnitude of yield stress enhancement by H exhibited its peak at 298 K (Fig. 4). Such a maximization of yield/flow stresses under a certain temperature range, which cannot be interpreted in the thermal activation theory of solid-solution hardening, is an outcome when dynamic interactions of solutes with moving dislocations operate [52,58].

Sills and co-workers numerically calculated the interference between a diffusible solute atmosphere and a dislocation moving at a constant velocity [35,51]. Based on Orowan's formula [62], they derived the equation describing the critical strain rates, $\dot{\varepsilon}_c$, for the occurrence of dynamic interactions under a given temperature.

$$\dot{\varepsilon}_c = \frac{4QDkT}{M\beta}\rho_\mathrm{m} b \tag{8}$$

where M is the Taylor factor (3.06 for polycrystalline FCC metals), k is the Boltzmann constant, β is defined by eq. (6), and ρ_m is the mobile dislocation density. The parameter Q signifies the velocity of mobile dislocations, v_d, which is non-dimensionalized using β,

D, k, and T as:

$$Q = \frac{v_{\mathrm{d}}\beta}{4DkT} \tag{9}$$

According to their calculations on a steady-state condition, the dislocation is completely pulled away from the solute atmosphere when Q is greater than $\approx 10^2$. Meanwhile, when Q is smaller than $\approx 10^{-2}$, the atmosphere can follow the dislocation movement with maintaining its near-equilibrium distribution [35]. These two opposite extremes will be referred to as breakaway and equilibrium limits, respectively. At a dislocation velocity between breakaway and equilibrium limits, the atmosphere partially lags behind the dislocation. A resultant non-equilibrium distribution of the atmosphere exerts a drag force on the moving dislocation, representing its maximum around $Q \approx 10^0$, which is consistent with the theoretical derivation by Cottrell [71].

$$\dot{\varepsilon}_c = \frac{4D\rho_{\mathrm{m}}b}{MI} \tag{10}$$

where I is the atmosphere radius that can be taken as $\approx 4b$ (see Fig. 10). Here, we parametrically simulated the feasibility of the solute drag by H atmosphere under $\rho_{\mathrm{m}} = 10^{10}$~$10^{13}$ m/m^3 using eq. (8)~(10), as well as the diffusivity data by Perng and Altstetter [79] shown in Fig. 9 (a). Although an accurate determination of ρ_{m} is difficult, it has been invoked by correlating the experimental stress-strain curve to theoretical equations that ρ_{m} promptly augments from 10^{10} to 10^{13} m/m^3 orders in ASS and FCC metals around the yield point [93,94]. It has been clarified that the Q-based criterion is applicable to extended dislocations, albeit the magnitude of drag force is slightly changed [51].

Fig. 11 shows the breakaway ($Q = 10^2$) and equilibrium ($Q = 10^{-2}$) limits at $\rho_{\mathrm{m}} = 10^{10}$, 10^{11}, 10^{12}, and 10^{13} m/m^3 calculated by eq. (9) as a function of temperature, in addition to the $\dot{\varepsilon}_c$ at the maximum steady-state drag force *via* eq. (10). The black horizontal lines at the middle height denote our base strain rate of 5×10^{-5}/s. In metallic materials, dislocation motion is more or less jerky [95], while eq. (10) only describes an average velocity, including the waiting time at internal obstacles such as forest dislocations. Therefore, when considering the true velocity in their motion between the obstacles, the three curves corresponding to $Q = 10^2$, 10^0, and 10^{-2} in Fig. 11 may lay at a somewhat lower strain rate in practice.

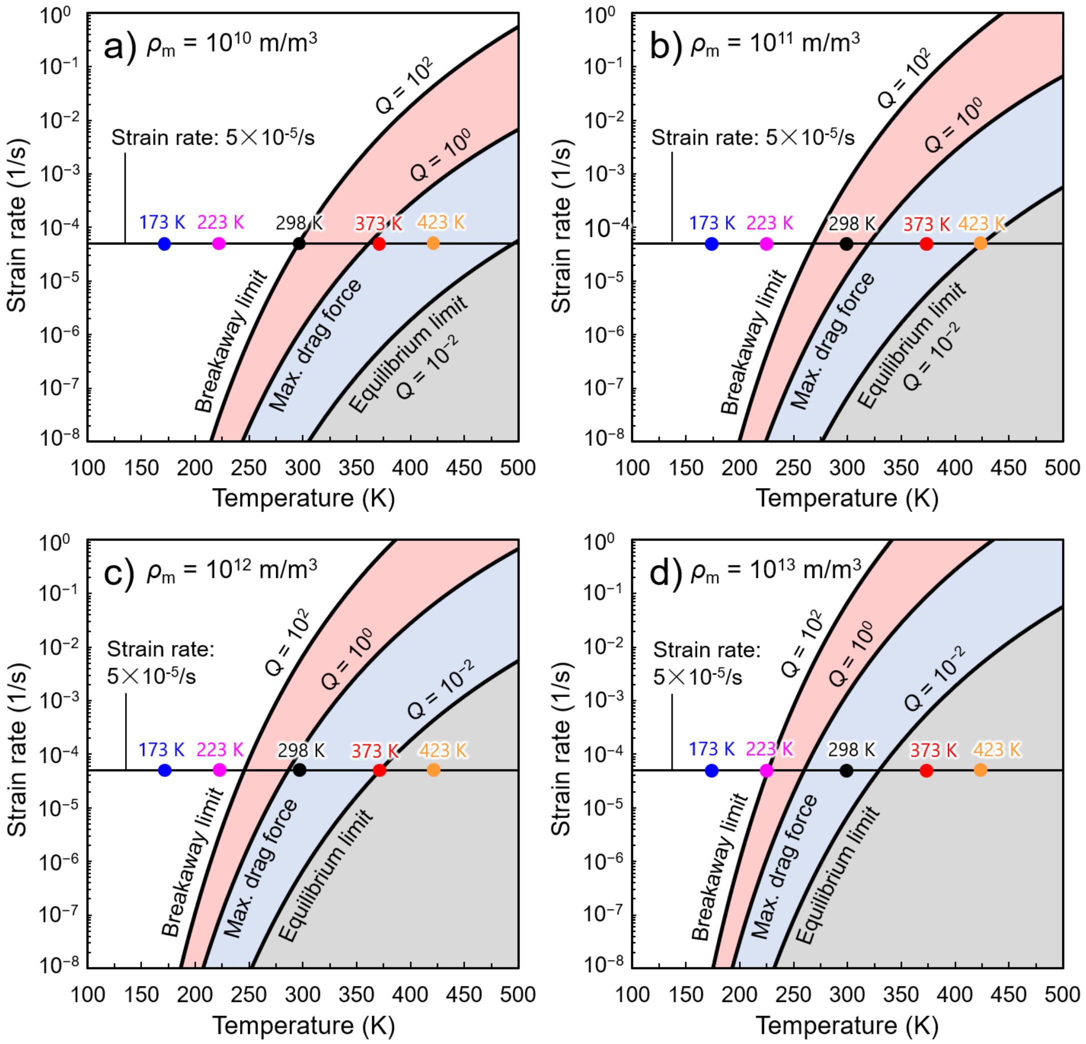

Fig. 11 Critical strain rates characterizing the diffusible hydrogen-mobile dislocation interactions, which are defined by $Q = 10^2$ and 10^{-2} in eq. (8)(9) as well as by eq. (10), as a function of temperature. The mobile dislocation density, ρ_m, is set as (a) 10^{10}, (b) 10^{11}, (c) 10^{12}, and (d) 10^{13} m/m^3. The black horizontal lines at the middle height in each diagram correspond to the base strain rate used in this study: 5×10^{-5}/s.

A numerical simulation performed by Yoshinaga and Morozumi has shown that the drag force exerted by solutes abruptly increases upon the dislocation velocity falling below the breakaway limit (Q = 10^2-10^0, red-shaded area in Fig. 11), then gradually decreases and asymptotically reaches zero after undergoing its peak ($Q = 10^0$-10^{-2}, blue-shaded area in Fig. 11) [72,96]. In view of this, the most remarkable situation in Fig. 11 is 298 K, where deformation starts near $Q = 10^2$ and proceeds to $Q = 10^{-2}$ *via* $Q = 10^0$. This means that the drag force suddenly augments at the beginning of deformation, followed by a gradual decrease in association with the multiplication and slowing down of mobile dislocations. Assuming that the drag force significantly contributes to the hardening caused by solute H, it is important to note that the reduction in the flow stress gap at 298 K with the increase of strain (Fig. 5 (f)) now seems a plausible consequence. Furthermore, the linearity of the yield stress enhancement at 298 K (Fig. 7 (a)) can somehow be attributed to the results [29,72,97,98] reporting that the drag force is proportional to the average solute concentration, albeit the hardening is aided by other factors discussed below. Conversely, no coordinative motion between diffusible H and mobile dislocations is feasible near the yield point at 173~223 K or under a faster strain rate of 5×10^{-3}/s at 298 K. Besides, dislocation velocity soon falls around and below the equilibrium limit at 423 K as well as at 298 K with the strain rate of 5×10^{-7}/s. These are potential rationales of the strain-independent flow stress gaps at those conditions (Fig. 5 (f)) and weaker yield stress enhancement at 298 K under strain rates of $5\times10^{-7}$and 5×10^{-3}/s (Fig. 4 (b)). From Fig. 11, the emergence of drag force around the yield point is somewhat anticipated at 373 K. This appears in a slight decay of the flow stress gap with the progress of deformation at 373 K (Fig. 5 (f)).

The decreasing magnitude of H-induced hardening after yielding at 298 K (Fig. 5 (f)) and temporal decrease in work-hardening rate (Fig. 5 (c)) can also be attributed to the yield point theory proposed by Johnston and Gilman (J-G) [99]. Since the dislocation velocity obeys a power low of the applied shear stress, τ, (*i.e.*, $v_d = (\tau/\tau_0)^m$ where τ_0 and m are material parameters [62]), a sudden increase in ρ_m leads to a deceleration of v_d (cf. eq. (8)(9)) and a resultant decrease in the flow stress under a constant strain rate. In materials with relatively high dislocation mobility, the plastic strain rate is controlled by the multiplication rate of dislocations instead of their individual velocity [100]. A typical example is FCC metals, in which dislocations activity is predominated by extrinsic obstacles (*e.g.*, forest dislocations) rather than intrinsic lattice frictions (*e.g.*, Peierls-Nabbaro potential) that render dislocations glide more viscous. Under such a circumstance, the J-G type yielding is unlikely to appear because the microscopic strain rate induced by each mobile dislocation promptly exceeds the macroscopic strain rate once the multiplication of dislocations commences [100,101]. The activation volume of dislocation motion up to hundreds of b^3 has been measured for the 310S steel at ambient temperature [5,20]. Even though these values are smaller than pure FCC metals (*i.e.*, thousands of b^3) and imply the involvement of intrinsic resistances by the presence of alloying elements, they are still larger compared with the conditions where the Peierls-

Nabbaro mechanism works significantly (*i.e.*, less than 100b^3) [58,102,103]. However, things may change as the dislocation movement becomes slower and more viscous under the influence of solute drag: when the multiplication rate is also controlled by the mobility of individual dislocations. Indeed, a smooth yield point discontinuity owing to the solute drag was confirmed in the high-temperature deformation of Al-Mg alloys [104,105], a phenomenon possibly applicable to our present case of an H-alloyed ASS. In reference [104,105], an evident yield drop was identified, while the H-charged ASS in this study retained a positive work-hardening rate (Fig. 5 (c)). This present result stems from a large work-hardening that overwhelms the stress drop due to the slowing down of dislocations: a different situation from [104,105], where work-hardening is negligible owing to the high homologous temperature. Note that the J-G type yielding at 298 K can seemingly be ascribed to the pinning of dislocation by the H-Cottrell atmosphere (Fig. 10 (b)) [4,5]. Nevertheless, the pinning effect cannot explain the lowing of yield stress by the strain rate augmentation (Fig. 4 (b)).

4.5 Implication of dynamic pinning

It is worth noting that higher yield and flow stresses were measured at 223 K than at 173 K (Fig.4 (b); Fig. 5 (f)), even though solute drag around the yield point is not anticipated (Fig. 11). Therefore, a different form of dynamic interaction should now be considered. One potential mechanism is the re-segregation of H atoms at the resting mobile dislocations at obstacles, pinning the dislocation when it attempts to move again (*i.e.*, DSA [56,73,74]). Although a coordinative motion between H and dislocation is infeasible at 223 K, a decent jump frequency up to 10^2/s (Fig. 9 (b)) might make it possible to segregate around a stationary dislocation and form an atmosphere in a relatively short time frame. In fact, a calculation by eq. (7) estimates the time for re-segregation to the dislocation core as only a few seconds, rationalizing the dynamic pinning under a slow strain rate situation. Another possibility is the formation of H-vacancy complexes through the deformation [106], which has analytically and experimentally been reported to pin the mobile dislocations [107,108] as with the case of DSA by C/N-vacancy complexes in ASSs [109]. Albeit, since the obstruction strength *via* these specific interactions might be marginal, it could easily be surmounted by thermal activation. The pinning by H-atmosphere supposedly contributed to the thermal component of flow stress at 223 K, whereas it became not influential as the lowering of strain rate and increasing temperature.

4.6 Lattice friction by dispersed hydrogen atoms

Except for the yielding domain at 298 K and a special case at 223 K, the H-induced flow stress enhancement was monotonically augmented with the decrease in temperature (Fig. 5 (f)). Moreover, after a true strain of 0.05, the flow stress enhancement was positively correlated with an increase in strain rate at 298 K (Fig. 5 (f)). These findings intimate that the H atoms dispersed into the matrix worked as short-range obstacles to amplify the thermal component of flow stress, which particularly played an important role when dynamic interactions (Sections 4.4 and 4.5) were not effective and thermal vibration of the lattice was marginal. Such a thermal behavior caused by dispersed H has recently been pointed out by Koyama et al. for HEAs [15]. The strengthening of ASSs by dispersed interstitials is typified by C and N, wherein short-range lattice dilation around them is a root cause of the dislocation obstructing effect [22,25,110,111]. A volume expansion by C was determined as 8.6×10^{-30} m^3 [22], an almost fourfold greater value than the lattice swelling by H dissolved in an O-site [86,87]. The dilation by N is even larger than C [22], giving rise to a query about how tiny atoms like H provoke a substantial hardening over tens of MPa.

The internal friction studies by Gavriljuk et al. and other researchers uncovered the Snoek-type relaxation peaks in cathodically or thermally H-charged ASSs (*e.g.*, Fe–25Cr–20Ni and Fe–18Cr–15Ni) [48–50,90,112,113]. Some of them ascribed the peak to a tetragonal lattice distortion stemming from H–H pairs in adjacent O-sites or substitutional-H pairs comprising Cr-H or Ni-H. Assuming Cr–H pairs as the primary cause of the Snoek peak, recent analytical claims inferring a strong affinity of Cr with H [87,114] can be reinforced. This idea also supports the previous results exhibiting the augmentation of H solubility and H-induced hardening capability with increasing the Cr content in the Fe-Cr-Ni alloy system [11,21,50]. In general, lattice strain by interstitial atoms in an O-site of FCC lattice is isotropic, interacting only with edge dislocation components that possess hydrostatic stress in their environs. On the contrary, the shear stress due to the anisotropic strain field around Cr–H pairs may interact with both edge and screw, thereby could work as a predominant piece for the hardening effect related to H atoms statistically dispersed in the lattice. Even for C and N, there is an argument that lattice dilation is not sufficient to explain the large strengthening by these elements; thereby, the contribution of interstitial-substitutional complexes should be considered [24,115]. Assuming that the Cr-H pairs are randomly dispersed at temperatures around 298 K, the average interspacing between each H atom in our experiments is estimated to be $b/(C_0)^{1/3}$ = 1~2 nm, letting a dislocation line to simultaneously interact with plural obstacles due to their extremely dense distribution. Under such a circumstance, the linear dependence of flow stress on the average solute concentration is envisaged [29], which further rationalizes the tendency in Fig. 7 (a).

Our stress relaxation tests at 298 K identified the presence of a thermal component of the flow stress, which might be related to dispersed H atoms or partially to the pinning of resting mobile dislocations by re-segregated H (Section 4.5). The rate of relaxation from a fixed strain of 0.06 became higher by the presence of H, while the stresses in non-charged and H-charged specimens asymptotically approached each other when the relaxation curves were extrapolated (Fig. 8). This means that the activity of dislocations lagged in the continuous straining due to the introduction of weak and more thermally activatable obstacles, *i.e.*, H, catching up later during the crosshead holding with the aid of time. The same physical meaning can be acquired from an increased strain rate sensitivity and a reduction in activation volume in H-charged ASSs [5,20].

The increase in stress relaxation rate (or creep rate) and reduced activation volume after H introduction has been attributed to the H-induced enhancement of thermally activated dislocation motion [5,20,57,116]. However, it seems a superficial interpretation disregarding that the relaxation was started at a fixed strain where the absolute stress level at the beginning was higher in the H-charged sample. Indeed, the creep tests from fixed stress carried out by Tien and Altstetter demonstrated a decreased creep rate at the initial short transient and, conversely, a longer creep duration in an H-doped 310S ASS [116]. These are clear evidence for the role of solute H that impedes the dislocation movement and renders the deformation more sluggish under a given driving force (*i.e.*, applied stress). Care is also required for understanding the magnitude of activation volume because the parameter is determined by the combination of multiple obstacles with various strengths, including alloying elements, dislocation intersections, precipitates, and, obviously, solute H [54,55,117,118]. Curtin theoretically stated that when more than two obstruction mechanisms cooperate, the activation area and enthalpy are primarily dominated by either of the obstacles that are more easily thermally activated than others [118]. In this regard, the smaller activation volume in the H-charged ASSs and FCC metals [5,20,57] might mainly stem from H itself (the weakest obstacle), whereas it is rooted in substitutional solutes as well as forest dislocations in the non-charged specimen.

4.7 Pinning by hydrogen atmosphere and low-temperature hardening

The significance of dislocation pinning by H atmosphere was denied at 298 K since the yield stress exhibited an inverse strain rate sensitivity when the strain rate was increased from 5×10^{-5} to 5×10^{-3}/s (Fig. 4 (b)). Because the radius of the atmosphere is a mere ~4b (Fig. 10 (e)), the core is unsaturated by H (Fig. 10 (d)), and the H atoms are mobile, it is envisaged that dislocations might be able to readily overcome the pinning even if it existed. Nevertheless, such insignificance of the atmosphere pinning shall not be applied when the solute H concentration is extremely high over a few at %.

Altstetter and co-workers identified the appearance of a distinct yield point in a room temperature tensile test with the strain rate of 5.5×10^{-5}/s when a 310S steel was cathodically charged with more than 4 at % H [4–6]. The H concentrations in their experiments (C_0 = 3.7, 5.3, and 7.2 at %) were adopted into eq. (4), a result of which is included in Fig. 10 (d) and (e). As the C_0 exceeds 5.3 at %, the core is saturated, and the atmosphere radius extends over 10b. Under these extreme conditions, the pinning by the atmosphere turns into a substantial magnitude [119], which impacts the H-induced enhancement of yield stress at 298 K. Such strong pinning inherently causes the decrease of initially mobile dislocation density. Thus, the dislocations, which once broke away from the pinning at the yield point, must rapidly move and multiply so that the specimen's gauge length conforms to the externally applied strain rate. Ultimately, the scenario forces depinning and subsequent fast movement for dislocations rather than their viscous motion accompanying solute drag. This might be the rationale for the abrupt yield drop observed at high C_0 in [4–6] instead of the smooth reduction of the flow stress enhancement in the present study (Fig. 5 (f)).

Hypothesizing the pinning by H atmosphere, the core saturation, and large atmosphere radius (*i.e.*, more than 6b) at 173 K under the C_0 up to 7570 at ppm is worthy of attention (Fig. 10 (d) and (e)). Since the aid of thermal activation for breaking away from the atmosphere fades exponentially at low temperatures, it is quite likely that the expected strong pinning of dislocations acted as a primary factor for determining the yield stress at 173 K. Moreover, as the partial dislocations separation increases at low temperatures and solute H is known to decrease stacking fault energy in ASSs [120,121], the chemical locking by segregated hydrogen, *i.e.*, Suzuki locking [29,122], is an anticipated outcome as well. Actually, the static strain-aging experiments performed by Girardin and Delafosse elegantly demonstrated the H-induced dislocations pinning at 173 K and its amplification by aging time in pure Ni and a Ni-Cr alloy with ~1900 at ppm H [42]. The H-induced dislocations pinning by their atmosphere or Suzuki locking were also inferred by room temperature internal friction measurements on Fe-18Cr-Ni alloys at a high vibrational frequency [89,112]. Fig. 4 (b) and Fig. 5 (f) notably revealed no influence of strain rate on the yield stress at 173 K when C_0 = 7570 at ppm. This means that most parts of the work required for surmounting the atmosphere pinning were supplied by an external force [58,62]. In this context, the prompt reduction in the flow stress enhancement immediately after the yielding at 173 K (Fig. 6 (c)) can now be considered a sign of dislocations depinning from their H atmosphere. The concentrated atmosphere is left behind the dislocation and cannot readily diffuse at low temperatures; the matrix H concentration was supposedly not enough under a small C_0 such as 2030 at ppm. Accordingly, the drop of the flow stress enhancement continued during a certain range of strain (Fig. 6 (c)). On the contrary, the matrix might also contain a significant amount of dispersed H atoms at a high C_0, *e.g.*, 7570 at ppm, obstructing the dislocations even after the depinning so as no further flow stress drop to persist in the course of straining (Fig. 6 (c)).

Other two striking distinctions at 173 K should be treated finally: H-induced yield stress enhancement increased as an apparently exponential function of C_0 (Fig. 7 (b)); the flow stress enhancement after yielding possessed an athermal character and did not depend on strain rate (Fig. 5 (e)). Although these features still have room for argument, the atmosphere distributions shown in Fig. 10 give a clue to the former if one assumes that the yield stress at 173 K was predominated by the dislocation depinning mechanism. Barnett et al. theoretically treated the pinning force by the Fermi-Dirac atmosphere with consideration of thermally activated breakaway and emphasized that the probability of breakaway is determined by the atmosphere radius besides the local solute concentration in the core [119]. In this regard, the aid of thermal activation might be somewhat helpful to facilitate the depinning at a lower C_0 (2030~5630 at ppm) where the extension of the atmosphere is smaller (Fig. 10 (e)), while it was not so influential at $C_0 = 7570$ at ppm. In a conventional dislocation theory considering the size effect, the maximum stress for the breakaway from the Cottrell atmosphere without any thermal activation, a large part of which comes from the solute segregation in or adjacent to the core, is proportional to the bulk solute concentration, C_0 [29]. Moreover, it seems in Fig. 10 (e) that the atmosphere also extends almost proportionally to C_0. Simply assuming these two are multipliable to determine the zero-temperature activation energy in a dislocation force-distance profile, the required stress for surmounting the obstacle should increase exponentially to C_0 when the energy supplied by thermal fluctuation is fixed, *i.e.*, at the same temperature.

An athermal hardening at low temperatures in which solutes are unlikely to diffuse has typically been observed in N-strengthened ASSs [23]. The phenomenon was ascribed to the presence of short-range order (SRO) comprising Cr-N aggregates [24,123,124], escalating the work for shear deformation corresponding to the formation energy of anti-phase boundaries [29,125]. The authors recently performed *Ab*-initio calculations to investigate the H absorption energies in an O-site of FCC iron by partially substituting the surrounding atoms with Ni and Cr [126]. Great reductions of the absorption energies manifested when one or two Cr atoms were located adjacent to the O-site, a consequence that stemmed from electronic interactions between H and Cr. On the basis of this affinity of H with Cr, one can expect the presence of Cr-H SRO in the Fe-Cr-Ni alloy system in a similar manner to Cr-N SRO [123,124] at the region where a high concentration of Cr is statistically clustered. During the cooling process to 173 K, H atoms might be preferentially coordinated at the O-sites adjacent to Cr, then frozen in due to the low diffusion coefficient. The athermal nature of H-induced hardening at 173 K appeared in the short transient stress relaxation (the inset in Fig. 8 (a)) as well, where relaxation curves in non-charged and H-charged specimens were close to each other, a case distinct from that at 298 K. Nonetheless, such athermal obstacles could not completely be stable owing to the still non-negligible jump frequency of H up to 10^{-2}/s (Fig. 9 (b)), inferring the collapse and reconstruction of the SRO zones during the time scale greater than 10^2 s. This led to the greater stress relaxation rate in the H-charged specimen at 173 K after the passage of 10^2 s (Fig. 8 (a)).

5. Summary and conclusion

The solid-solution hardening by H was studied at 173~423 K and two different strain rates: 5×10^{-5} and 5×10^{-3} /s in Fe-24Cr-19Ni-based ASS charged with 2000~7600 at ppm H, resulting in the main experimental findings as follows.

1. The hardening was maximized at 298 K under the slow strain rate condition of 5×10^{-5} /s, where the magnitude of yield stress enhancement was a linear function of the H concentration. Nonetheless, the extent of strengthening decayed as the strain increased.
2. The hardening was still significant at the lower temperatures, such as 173 K and 223 K, yet its concentration dependence was not linear but rather relatively exponential at 173 K.
3. Above 373 K, the hardening was minimized and became negligible at 423 K.

Ultimately, the rationales for the strengthening were discussed in terms of four essential ingredients: (i) H atoms in the lattice as dispersed obstacles; (ii) pinning of stationary dislocations by H atmosphere; (iii) dynamic pinning of dislocations resting at obstacles; (iv) drag force to moving dislocations by migratable H clouds. In Table 2 and Fig. 12, the feasibilities of these (i)~(iv) under the test conditions in this study are summarized, in addition to the schematic strengthening mechanism map as functions of strain rate and temperature. (i), (iii), and (iv) predominated the yield and flow stress around ambient temperature, albeit their individual significance was changed depending on the strain rate. Meanwhile, as the temperature decreased below 200 K, (i) and (ii) became more essential contributors due to the low diffusivity of H and weak thermal fluctuation. With the aid of enhanced thermal activation and fast diffusion of H, all the (i)~(iv) were diminished, resulting in the absence of strengthening at high-temperatures above 400 K.

Table 2 Summary of the strengthening factors under each testing condition.

<table>
<tr><th>Temp.</th><th>Strain rate (1/s)</th><th>(i) Dispersed Obstacles</th><th>(ii) Static Pinning</th><th>(iii) Dynamic Pinning</th><th>(iv) Atmosphere Drag Force</th></tr>
<tr><td rowspan="2">Low
(< 200 K)</td><td>5×10^{-5}</td><td rowspan="2">Significant for flow stress (Athermal)</td><td rowspan="2">Significant for yield stress (Themal/Athermal)</td><td rowspan="2" colspan="2">Absent
(H is not diffusible)</td></tr>
<tr><td>5×10^{-3}</td></tr>
<tr><td rowspan="2">Medium
(≈ 300 K)</td><td>5×10^{-5}</td><td>Moderate (Thermally activated)</td><td rowspan="2">Trivial (Thermally activated)</td><td rowspan="2">Moderate (Thermally activated)</td><td>Significant for yield stress</td></tr>
<tr><td>5×10^{-3}</td><td>Significant</td><td rowspan="3">Absent (Breakaway or equilibration of atmosphere)</td></tr>
<tr><td rowspan="2">High
(> 400 K)</td><td>5×10^{-5}</td><td rowspan="2" colspan="3">Trivial
(Thermally activated)</td></tr>
<tr><td>5×10^{-3}</td></tr>
</table>

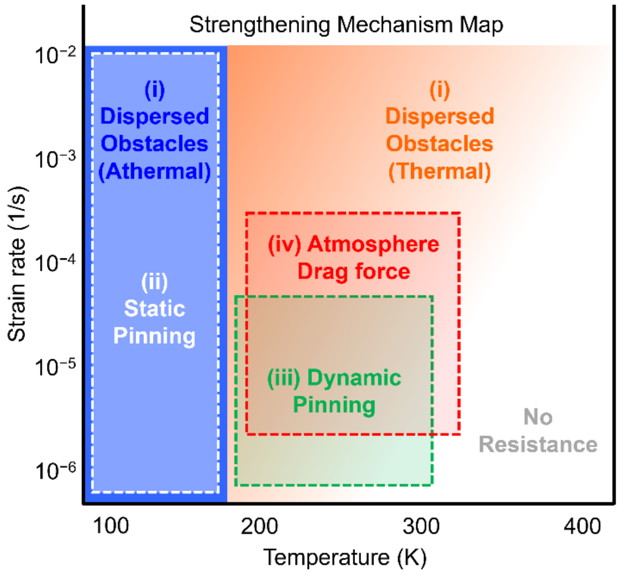

Fig. 12 Schematic illustration of the predominant H-induced strengthening mechanisms in austenitic steel with the H concentration up to 7600 at ppm under the given strain rate and temperature conditions.

Acknowledgments

This work was supported by JSPS KAKENHI (Grant Numbers: 21K14045 and 21K04702). YO would also like to acknowledge financial support from JFE 21st Century Foundation and The Iwatani Naoji Foundation. The authors are grateful to the members of the Kobe Materials Testing Laboratory (KMTL) group, Japan, for their careful support in the experiments performed in this study.

Data availability

The raw/processed data required to reproduce these findings cannot be shared at this time as the data also forms part of an ongoing study.

References

[1] T. Boniszewski, G.C. Smith, The influence of hydrogen on the plastic deformation ductility, and fracture of nickel in tension, Acta Metallurgica. 11 (1963) 165–178. https://doi.org/10.1016/0001-6160(63)90209-8.

[2] J.S. Blakemore, The Portevin-Le Chatelier Effect in hydrogenated nickel, Metallurgical Transactions. 1 (1970) 145–149. https://doi.org/10.1007/BF02819254.

[3] J.S. Blakemore, The portevin-le chatelier effect in hydrogenated nickel alloys, Metallurgical and Materials Transactions. 1 (1970) 151–156. https://doi.org/10.1007/BF02819255.

[4] D.P. Abraham, C.J. Altstetter, The effect of hydrogen on the yield and flow stress of an austenitic stainless steel, Metallurgical and Materials Transactions A. 26 (1995) 2849–2858. https://doi.org/10.1007/BF02669643.

[5] D.P. Abraham, C.J. Altstetter, Hydrogen-enhanced localization of plasticity in an austenitic stainless steel, Metallurgical and Materials Transactions A. 26 (1995) 2859–2871. https://doi.org/10.1007/BF02669644.

[6] D.G. Ulmer, C.J. Altstetter, Hydrogen-induced strain localization and failure of austenitic stainless steels at high hydrogen concentrations, Acta Metallurgica et Materialia. 39 (1991) 1237–1248. https://doi.org/10.1016/0956-7151(91)90211-I.

[7] O. Takakuwa, Y. Mano, H. Soyama, Increase in the local yield stress near surface of austenitic stainless steel due to invasion by hydrogen, Int J Hydrogen Energy. 39 (2014) 6095–6103. https://doi.org/10.1016/j.ijhydene.2014.01.190.

[8] K. Wada, J. Yamabe, H. Matsunaga, Mechanism of hydrogen-induced hardening in pure nickel and in a copper–nickel alloy analyzed by micro Vickers hardness testing, Materials Science and Engineering: A. 805 (2021) 140580. https://doi.org/10.1016/j.msea.2020.140580.

[9] K. Nibur, D. Bahr, B. Somerday, Hydrogen effects on dislocation activity in austenitic stainless steel, Acta Mater. 54 (2006) 2677–2684. https://doi.org/10.1016/j.actamat.2006.02.007.

[10] V.G. Gavriljuk, V.N. Shivanyuk, J. Foct, Diagnostic experimental results on the hydrogen embrittlement of austenitic steels, Acta Mater. 51 (2003) 1293–1305. https://doi.org/10.1016/S1359-6454(02)00524-4.

[11] D.M. Symons, Hydrogen embrittlement of Ni-Cr-Fe alloys, Metallurgical and Materials Transactions A. 28 (1997) 655–663. https://doi.org/10.1007/s11661-997-0051-4.

[12] K. Wada, J. Yamabe, Y. Ogawa, O. Takakuwa, T. Iijima, H. Matsunaga, Comparative study of hydrogen-induced intergranular fracture behavior in Ni and Cu–Ni alloy at ambient and cryogenic temperatures, Materials Science and Engineering A. 766 (2019) 138349. https://doi.org/10.1016/j.msea.2019.138349.

[13] K. Ichii, M. Koyama, C.C. Tasan, K. Tsuzaki, Comparative study of hydrogen embrittlement in stable and metastable high-entropy alloys, Scr Mater. 150 (2018) 74–77. https://doi.org/10.1016/j.scriptamat.2018.03.003.

[14] K.E. Nygren, K.M. Bertsch, S. Wang, H. Bei, A. Nagao, I.M. Robertson, Hydrogen embrittlement in compositionally complex FeNiCoCrMn FCC solid solution alloy, Curr Opin Solid State Mater Sci. 22 (2018) 1–7. https://doi.org/10.1016/j.cossms.2017.11.002.

[15] M. Koyama, K. Ichii, K. Tsuzaki, Strain Rate and Temperature Effects on Hydrogen Embrittlement of Stable and Metastable High-Entropy Alloys, Physical Mesomechanics. 25 (2022) 385–392. https://doi.org/10.1134/S1029959922050010.

[16] Q. Sun, J. He, A. Nagao, Y. Ni, S. Wang, Hydrogen-prompted heterogeneous development of dislocation structure in Ni, Acta Mater. 246 (2023) 118660. https://doi.org/10.1016/j.actamat.2022.118660.

[17] M.B. Djukic, G.M. Bakic, V.S. Zeravcic, A. Sedmak, B. Rajicic, Hydrogen embrittlement of industrial components: Prediction, prevention, and models, Corrosion. 72 (2016) 943–961.

https://doi.org/10.5006/1958.

[18] H.K.D.H. Bhadeshia, Prevention of Hydrogen Embrittlement in Steels, ISIJ International. 56 (2016) 24–36. https://doi.org/10.2355/isijinternational.ISIJINT-2015-430.

[19] S. Lynch, Hydrogen embrittlement phenomena and mechanisms, Corrosion Reviews. 30 (2012) 105–123. https://doi.org/10.1515/corrrev-2012-0502.

[20] Y. Ogawa, H. Hosoi, K. Tsuzaki, T. Redarce, O. Takakuwa, H. Matsunaga, Hydrogen, as an alloying element, enables a greater strength-ductility balance in an Fe-Cr-Ni-based, stable austenitic stainless steel, Acta Mater. 199 (2020) 181–192. https://doi.org/10.1016/j.actamat.2020.08.024.

[21] H. Nishida, Y. Ogawa, K. Tsuzaki, Chemical composition dependence of the strength and ductility enhancement by solute hydrogen in Fe–Cr–Ni-based austenitic alloys, Materials Science and Engineering: A. 836 (2022) 142681. https://doi.org/10.1016/j.msea.2022.142681.

[22] H.M. Ledbetter, M.W. Austin, Dilation of an fcc Fe–Cr–Ni alloy by interstitial carbon and nitrogen, Materials Science and Technology (United Kingdom). 3 (1987) 101–104. https://doi.org/10.1179/mst.1987.3.2.101.

[23] M.L.G. Byrnes, M. Grujicic, W.S. Owen, Nitrogen strengthening of a stable austenitic stainless steel, Acta Metallurgica. 35 (1987) 1853–1862. https://doi.org/10.1016/0001-6160(87)90131-3.

[24] K. Oda, N. Kondo, X-ray Absorption Fine Structure Analysis of Interstitial (C, N)-Substitutional (Cr) complexes in Austenitic stainless steels, ISIJ International. 30 (1990) 625–631.

[25] N. Ohkubo, K. Miyakusu, Y. Uematsu, H. Kimura, Effect of Alloying Elements on the Mechanical Properties of the Stable Austenitic Stainless Steel., ISIJ International. 34 (1994) 764–772. https://doi.org/10.2355/isijinternational.34.764.

[26] R.P. Reed, Nitrogen in austenitic stainless steels, JOM. 41 (1989) 16–21. https://doi.org/10.1007/BF03220991.

[27] R.L. Fleischer, Solution hardening, Acta Metallurgica. 9 (1961) 996–1000. https://doi.org/10.1016/0001-6160(61)90242-5.

[28] F.R.N. Nabarro, The theory of solution hardening, Philosophical Magazine. 35 (1977) 613–622. https://doi.org/10.1080/14786437708235994.

[29] P.M. Anderson, J.P. Hirth, J. Lothe, Theory of Dislocations, 3rd ed., Cambridge University Press, 2017.

[30] M.Z. Butt, P. Feltham, Solid-solution hardening, J Mater Sci. 28 (1993) 2557–2576. https://doi.org/10.1007/BF00356192.

[31] N.F. Mott, F.R.N. Nabarro, Dislocation theory and transient creep, in: Physical Society Bristol Conference Report, 1948: pp. 1–19.

[32] H.K. Birnbaum, P. Sofronis, Hydrogen-enhanced localized plasticity—a mechanism for hydrogen-related fracture, Materials Science and Engineering: A. 176 (1994) 191–202. https://doi.org/10.1016/0921-5093(94)90975-X.

[33] J. Song, W.A. Curtin, Mechanisms of hydrogen-enhanced localized plasticity: An atomistic study using α-Fe as a model system, Acta Mater. 68 (2014) 61–69. https://doi.org/10.1016/j.actamat.2014.01.008.

[34] G. Girardin, C. Huvier, D. Delafosse, X. Feaugas, Correlation between dislocation organization and slip bands: TEM and AFM investigations in hydrogen-containing nickel and nickel–chromium, Acta Mater. 91 (2015) 141–151. https://doi.org/10.1016/j.actamat.2015.03.016.

[35] E.N. Epperly, R.B. Sills, Transient solute drag and strain aging of dislocations, Acta Mater. 193 (2020) 182–190. https://doi.org/10.1016/j.actamat.2020.03.031.

[36] H.K. Birnbaum, Hydrogen effects on deformation — Relation between dislocation behavior and the macroscopic stress-strain behavior, Scripta Metallurgica et Materialia. 31 (1994) 149–153. https://doi.org/10.1016/0956-716X(94)90166-X.

[37] B.A. Wilcox, G.C. Smith, The Portevin-Le Chatelier effect in hydrogen charged nickel, Acta Metallurgica. 12 (1964) 371–376. https://doi.org/10.1016/0001-6160(64)90006-9.

[38] A.H. Windle, G.C. Smith, The Effect of Hydrogen on the Plastic Deformation of Nickel Single Crystals, Metal Science Journal. 2 (1968) 187–191.

https://doi.org/10.1179/030634568790443314.

[39] G.P.M. Leyson, B. Grabowski, J. Neugebauer, Multiscale description of dislocation induced nano-hydrides, Acta Mater. 89 (2015) 50–59. https://doi.org/10.1016/j.actamat.2015.01.057.

[40] Y. Tang, J.A. El-Awady, Atomistic simulations of the interactions of hydrogen with dislocations in fcc metals, Phys Rev B Condens Matter Mater Phys. 86 (2012) 1–13. https://doi.org/10.1103/PhysRevB.86.174102.

[41] J.E. Angelo, N.R. Moody, M.I. Baskes, Trapping of hydrogen to lattice defects in nickel, Model Simul Mat Sci Eng. 3 (1995) 289–307. https://doi.org/10.1088/0965-0393/3/3/001.

[42] G. Girardin, D. Delafosse, Measurement of the saturated dislocation pinning force in hydrogenated nickel and nickel base alloys, Scr Mater. 51 (2004) 1177–1181. https://doi.org/10.1016/j.scriptamat.2004.07.012.

[43] S. Wang, A. Nagao, K. Edalati, Z. Horita, I.M. Robertson, Influence of hydrogen on dislocation self-organization in Ni, Acta Mater. 135 (2017) 96–102. https://doi.org/10.1016/j.actamat.2017.05.073.

[44] P.J. Ferreira, I.M. Robertson, H.K. Birnbaum, Hydrogen effects on the character of dislocations in high-purity aluminum, Acta Mater. 47 (1999) 2991–2998. https://doi.org/10.1016/S1359-6454(99)00156-1.

[45] J.P. Chateau, D. Delafosse, T. Magnin, Numerical simulations of hydrogen–dislocation interactions in fcc stainless steels.: part I: hydrogen–dislocation interactions in bulk crystals, Acta Mater. 50 (2002) 1507–1522. https://doi.org/10.1016/S1359-6454(02)00008-3.

[46] I.M. Robertson, The effect of hydrogen on dislocation dynamics, Eng Fract Mech. 68 (2001) 671–692. https://doi.org/10.1016/S0013-7944(01)00011-X.

[47] S.K. Lawrence, Y. Yagodzinskyy, H. Hänninen, E. Korhonen, F. Tuomisto, Z.D. Harris, B.P. Somerday, Effects of grain size and deformation temperature on hydrogen-enhanced vacancy formation in Ni alloys, Acta Mater. 128 (2017) 218–226. https://doi.org/10.1016/j.actamat.2017.02.016.

[48] V.G. Gavriljuk, H. Haänninen, S.Y.U. Smouk, A. V. Tarasenko, K. Ullakko, Internal friction in hydrogen-charged CrNi and CrNiMn austenitic stainless steels, Metall Mater Trans A Phys Metall Mater Sci. 27 (1996) 1815–1821. https://doi.org/10.1007/BF02651931.

[49] S. Asano, M. Shibata, R. Tsunoda, Internal friction due to hydrogen in austenitic stainless steels, Scripta Metallurgica. 14 (1980) 377–382. https://doi.org/10.1016/0036-9748(80)90330-0.

[50] N. Ide, T. Naito, S. Asano, Internal friction peak in FCC Fe-Cr-Ni alloys hydrogen-charged by gas-equilibration method, Japanese Journal of Applied Physics, Part 1: Regular Papers and Short Notes and Review Papers. 44 (2005) 8088–8090. https://doi.org/10.1143/JJAP.44.8088.

[51] R.B. Sills, W. Cai, Solute drag on perfect and extended dislocations, Philosophical Magazine. 96 (2016) 895–921. https://doi.org/10.1080/14786435.2016.1142677.

[52] C.G. Schmidt, A.K. Miller, The effect of solutes on the strength and strain hardening behavior of alloys, Acta Metallurgica. 30 (1982) 615–625. https://doi.org/10.1016/0001-6160(82)90110-9.

[53] T. Suzuki, On the Studies of Solid Solution Hardening, Jpn J Appl Phys. 20 (1981) 449. https://doi.org/10.1143/JJAP.20.449.

[54] G. Laplanche, J. Bonneville, C. Varvenne, W.A. Curtin, E.P. George, Thermal activation parameters of plastic flow reveal deformation mechanisms in the CrMnFeCoNi high-entropy alloy, Acta Mater. 143 (2018) 257–264. https://doi.org/10.1016/j.actamat.2017.10.014.

[55] R.A. Mulford, Analysis of strengthening mechanisms in alloys by means of thermal-activation theory, Acta Metallurgica. 27 (1979) 1115–1124. https://doi.org/10.1016/0001-6160(79)90129-9.

[56] A. Van Den Beukel, U.F. Kocks, The strain dependence of static and dynamic strain-aging, Acta Metallurgica. 30 (1982) 1027–1034. https://doi.org/10.1016/0001-6160(82)90211-5.

[57] E. Sirois, H.K. Birnbaum, Effects of hydrogen and carbon on thermally activated deformation in nickel, Acta Metallurgica et Materialia. 40 (1992) 1377–1385. https://doi.org/10.1016/0956-7151(92)90438-K.

[58] D. Caillard, J.L. Martin, Thermally Activated Mechanisms in Crystal Plasticity, 1st ed., Pergamon, 2003.

[59] C. San Marchi, B. Somerday, S. Robinson, Permeability, solubility and diffusivity of hydrogen

isotopes in stainless steels at high gas pressures, Int J Hydrogen Energy. 32 (2007) 100–116. https://doi.org/10.1016/j.ijhydene.2006.05.008.

[60] H.M. Ledbetter, W.F. Weston, E.R. Naimon, Low-temperature elastic properties of four austenitic stainless steels, J Appl Phys. 46 (1975) 3855–3860. https://doi.org/10.1063/1.322182.

[61] U.F. Kocks, H. Mecking, Physics and phenomenology of strain hardening: the FCC case, Prog Mater Sci. 48 (2003) 171–273. https://doi.org/10.1016/S0079-6425(02)00003-8.

[62] D. Hull, D.J. Bacon, Introduction to Dislocations, 3rd ed., Butterworth-Heinemann, 2011. https://doi.org/10.1016/C2009-0-64358-0.

[63] I. Aubert, J.-M. Olive, N. Saintier, The effect of internal hydrogen on surface slip localisation on polycrystalline AISI 316L stainless steel, Materials Science and Engineering: A. 527 (2010) 5858–5866. https://doi.org/10.1016/j.msea.2010.05.062.

[64] P.J. Ferreira, I.M. Robertson, H.K. Birnbaum, Hydrogen effects on the interaction between dislocations, Acta Mater. 46 (1998) 1749–1757. https://doi.org/10.1016/S1359-6454(97)00349-2.

[65] I. Aubert, N. Saintier, J.-M. Olive, Crystal plasticity computation and atomic force microscopy analysis of the internal hydrogen-induced slip localization on polycrystalline stainless steel, Scr Mater. 66 (2012) 698–701. https://doi.org/10.1016/j.scriptamat.2012.01.019.

[66] K. Kamei, Y. Koumura, A. Macadre, K. Goda, Quantitative Evaluation of Solute Hydrogen Effect on Dislocation Density in a Low-carbon Stable Austenitic Stainless Steel, ISIJ International. 61 (2021) 1736–1738. https://doi.org/10.2355/isijinternational.ISIJINT-2020-677.

[67] Y. Ogawa, H. Nishida, O. Takakuwa, K. Tsuzaki, Hydrogen-enhanced deformation twinning in Fe-Cr-Ni-based austenitic steel characterized by in-situ EBSD observation, Mater Today Commun. 34 (2023) 105433. https://doi.org/10.1016/j.mtcomm.2023.105433.

[68] D.H. Lassila, H.K. Birnbaum, The effect of diffusive segregation on the fracture of hydrogen charged nickel, Acta Metallurgica. 36 (1988) 2821–2825. https://doi.org/10.1016/0001-6160(88)90128-9.

[69] S. Takaki, D. Akama, N. Nakada, T. Tsuchiyama, Effect of Grain Boundary Segregation of Interstitial Elements on Hall-Petch Coefficient in Steels, Mater Trans. 55 (2014) 28–34. https://doi.org/10.2320/matertrans.MA201314.

[70] Y. Mine, Z. Horita, Y. Murakami, Effect of high-pressure torsion on hydrogen trapping in Fe-0.01 mass% C and type 310S austenitic stainless steel, Acta Mater. 58 (2010) 649–657. https://doi.org/10.1016/j.actamat.2009.09.043.

[71] A. H. Cottrell, Dislocations and Plastic Flow in Crystals, Oxford Univ. Press, New York, 1953.

[72] H. Yoshinaga, S. Morozumi, The solute atmosphere round a moving dislocation and its dragging stress, The Philosophical Magazine: A Journal of Theoretical Experimental and Applied Physics. 23 (1971) 1367–1385. https://doi.org/10.1080/14786437108217008.

[73] R.A. Mulford, U.F. Kocks, New observations on the mechanisms of dynamic strain aging and of jerky flow, Acta Metallurgica. 27 (1979) 1125–1134. https://doi.org/10.1016/0001-6160(79)90130-5.

[74] J. Mola, G. Luan, Q. Huang, C. Ullrich, O. Volkova, Y. Estrin, Dynamic strain aging mechanisms in a metastable austenitic stainless steel, Acta Mater. 212 (2021) 116888. https://doi.org/10.1016/j.actamat.2021.116888.

[75] T. Tabata, H.K. Birnbaum, Direct observations of the effect of hydrogen on the behavior of dislocations in iron, Scripta Metallurgica. 17 (1983) 947–950. https://doi.org/10.1016/0036-9748(83)90268-5.

[76] S. Taketomi, R. Matsumoto, N. Miyazaki, Atomistic study of the competitive relationship between edge dislocation motion and hydrogen diffusion in alpha iron, J Mater Res. 26 (2011) 1269–1278. https://doi.org/10.1557/jmr.2011.106.

[77] R. Matsumoto, S.T. Oyinbo, M. Vijendran, S. Taketomi, Hydrogen Effect on the Mobility of Edge Dislocation in α-Iron: A Long-Timescale Molecular Dynamics Simulation, ISIJ International. 62 (2022) ISIJINT-2022-311. https://doi.org/10.2355/isijinternational.ISIJINT-2022-311.

[78] R. Matsumoto, S. Taketomi, Molecular dynamics simulation of Surface-Adsorbed-Hydrogen-

Induced Dislocation Motion in a thin film, Comput Mater Sci. 171 (2020) 109240. https://doi.org/10.1016/j.commatsci.2019.109240.

[79] P. Tsong-Pyng, C.J. Altstetter, Effects of deformation on hydrogen permeation in austenitic stainless steels, Acta Metallurgica. 34 (1986) 1771–1781. https://doi.org/10.1016/0001-6160(86)90123-9.

[80] Y. Mine, T. Kimoto, Hydrogen uptake in austenitic stainless steels by exposure to gaseous hydrogen and its effect on tensile deformation, Corros Sci. 53 (2011) 2619–2629. https://doi.org/10.1016/j.corsci.2011.04.022.

[81] Y. Yagodzinskyy, O. Todoshchenko, S. Papula, H. Hänninen, Hydrogen Solubility and Diffusion in Austenitic Stainless Steels Studied with Thermal Desorption Spectroscopy, Steel Res Int. 82 (2011) 20–25. https://doi.org/10.1002/srin.201000227.

[82] N.R. Quick, H.H. Johnson, Permeation and diffusion of hydrogen and deuterium in 310 stainless steel, 472 K to 779 K, Metallurgical Transactions A. 10 (1979) 67–70. https://doi.org/10.1007/BF02686408.

[83] J.P. Hirth, Effects of hydrogen on the properties of iron and steel, Metallurgical Transactions A. 11 (1980) 861–890. https://doi.org/10.1007/BF02654700.

[84] G. Lu, Q. Zhang, N. Kioussis, E. Kaxiras, Hydrogen-Enhanced Local Plasticity in Aluminum: An Ab Initio Study, Phys Rev Lett. 87 (2001) 095501. https://doi.org/10.1103/PhysRevLett.87.095501.

[85] C.G. Rhodes, A.W. Thompson, The composition dependence of stacking fault energy in austenitic stainless steels, Metallurgical Transactions A. 8 (1977) 1901–1906. https://doi.org/10.1007/BF02646563.

[86] D.G. Ulmer, C.J. Altstetter, Phase relations in the hydrogen-austenite system, Acta Metallurgica Et Materialia. 41 (1993) 2235–2241. https://doi.org/10.1016/0956-7151(93)90393-7.

[87] X.W. Zhou, C. Nowak, R.S. Skelton, M.E. Foster, J.A. Ronevich, C. San Marchi, R.B. Sills, An Fe–Ni–Cr–H interatomic potential and predictions of hydrogen-affected stacking fault energies in austenitic stainless steels, Int J Hydrogen Energy. 47 (2022) 651–665. https://doi.org/10.1016/j.ijhydene.2021.09.261.

[88] M.R. Louthan, G.R. Caskey, J.A. Donovan, D.E. Rawl, Hydrogen embrittlement of metals, Materials Science and Engineering. 10 (1972) 357–368. https://doi.org/10.1016/0025-5416(72)90109-7.

[89] A. Atrens, N.F. Fiore, K. Miura, Dislocation damping and hydrogen pinning in austenitic stainless steels, J Appl Phys. 48 (1977) 4247–4251. https://doi.org/10.1063/1.323410.

[90] Y. Yagodzinskyy, M. Ivanchenko, H. Hänninen, Hydrogen-Dislocation Interaction in Austenitic Stainless Steel Studied with Mechanical Loss Spectroscopy, Solid State Phenomena. 184 (2012) 227–232. https://doi.org/10.4028/www.scientific.net/SSP.184.227.

[91] M. Yamaguchi, M. Itakura, T. Tsuru, K. Ebihara, Hydrogen-Trapping Energy in Screw and Edge Dislocations in Aluminum: First-Principles Calculations, Mater Trans. 62 (2021) 582–589. https://doi.org/10.2320/matertrans.MT-M2020375.

[92] S. Harper, Precipitation of Carbon and Nitrogen in Cold-Worked Alpha-Iron, Physical Review. 83 (1951) 709–712. https://doi.org/10.1103/PhysRev.83.709.

[93] T.H. Alden, Theory of mobile dislocation density: Application to the deformation of 304 stainless steel, Metallurgical Transactions A. 18 (1987) 51–62. https://doi.org/10.1007/BF02646221.

[94] Y. Estrin, L.P. Kubin, Local strain hardening and nonuniformity of plastic deformation, Acta Metallurgica. 34 (1986) 2455–2464. https://doi.org/10.1016/0001-6160(86)90148-3.

[95] U.F. Kocks, A.S. Argon, M.F. Ashby, Thermodynamics and Kinetics of Slip, Prog Mater Sci. 19 (1975) 1–291. https://linkinghub.elsevier.com/retrieve/pii/0079642575900055.

[96] H. Yoshinaga, S. Morozumi, A Portevin-Le Chatelier effect expected from solute atmosphere dragging, The Philosophical Magazine: A Journal of Theoretical Experimental and Applied Physics. 23 (1971) 1351–1366. https://doi.org/10.1080/14786437108217007.

[97] B. Burton, The influence of solute drag on dislocation creep, Philosophical Magazine A. 46 (1982) 607–616. https://doi.org/10.1080/01418618208236916.

[98] R. Fuentes-samaniego, R. Gasca-Neri, J.P. Hirth, Solute drag on moving edge dislocations,

Philosophical Magazine A. 49 (1984) 31–43. https://doi.org/10.1080/01418618408233426.

[99] W.G. Johnston, J.J. Gilman, Dislocation velocities, dislocation densities, and plastic flow in lithium fluoride crystals, J Appl Phys. 30 (1959) 129–144. https://doi.org/10.1063/1.1735121.

[100] H. Saka, Classical Theory of Crystal Dislocations: From Iron to Gallium Nitride, World Scientific Pub Co Inc, 2017.

[101] K. Nakagawa, K. Maeda, S. Takeuchi, Plastic Deformation of CdTe Single Crystals. I. Microscopic Observations, J Physical Soc Japan. 49 (1980) 1909–1915. https://doi.org/10.1143/JPSJ.49.1909.

[102] A.H.W. Ngan, A new model for dislocation kink-pair activation at low temperatures based on the Peierls-Nabarro concept, Philosophical Magazine A. 79 (1999) 1697–1720. https://doi.org/10.1080/01418619908210387.

[103] A.G. Evans, R.D. Rawlings, The Thermally Activated Deformation of Crystalline Materials, Physica Status Solidi (b). 34 (1969) 9–31. https://doi.org/10.1002/pssb.19690340102.

[104] R. Horiuchi, H. Yoshinaga, Mechanism of the High Temperature Yield Point Phenomenon in Some Aluminium Alloys, Transactions of the Japan Institute of Metals. 6 (1965) 131–138. https://doi.org/10.2320/matertrans1960.6.131.

[105] R. Horiuchi, H. Yoshinaga, S. Hama, New Yielding Phenomenon in Some Aluminium Alloys at High Temperatures, Transactions of the Japan Institute of Metals. 6 (1965) 123–130. https://doi.org/10.2320/matertrans1960.6.123.

[106] M. Hatano, M. Fujinami, K. Arai, H. Fujii, M. Nagumo, Hydrogen embrittlement of austenitic stainless steels revealed by deformation microstructures and strain-induced creation of vacancies, Acta Mater. 67 (2014) 342–353. https://doi.org/10.1016/j.actamat.2013.12.039.

[107] Y. Zhu, Z. Li, M. Huang, H. Fan, Study on interactions of an edge dislocation with vacancy-H complex by atomistic modelling, Int J Plast. 92 (2017) 31–44. https://doi.org/10.1016/j.ijplas.2017.03.003.

[108] D. Xie, S. Li, M. Li, Z. Wang, P. Gumbsch, J. Sun, E. Ma, J. Li, Z. Shan, Hydrogenated vacancies lock dislocations in aluminium, Nat Commun. 7 (2016) 13341. https://doi.org/10.1038/ncomms13341.

[109] L.H. de Almeida, I. Le May, P.R.O. Emygdio, Mechanistic Modeling of Dynamic Strain Aging in Austenitic Stainless Steels, Mater Charact. 41 (1998) 137–150. https://doi.org/10.1016/S1044-5803(98)00031-X.

[110] Y. MURATA, S. OHASHI, Y. UEMATSU, Recent Trends in High Strength Stainless Steel, Tetsu-to-Hagane. 78 (1992) 346–353. https://doi.org/10.2355/tetsutohagane1955.78.3_346.

[111] E. Werner, Solid solution and grain size hardening of nitrogen-alloyed austenitic steels, Materials Science and Engineering: A. 101 (1988) 93–98. https://doi.org/10.1016/0921-5093(88)90054-8.

[112] S. Asano, K. Oshima, Effect of Plastic Deformation on the Hydrogen-Induced Internal Friction Peak in Austenitic Stainless Steel, Transactions of the Japan Institute of Metals. 23 (1982) 530–534. https://doi.org/10.2320/matertrans1960.23.530.

[113] Y. Yagodzinskyy, E. Andronova, M. Ivanchenko, H. Hänninen, Anelastic mechanical loss spectrometry of hydrogen in austenitic stainless steels, Materials Science and Engineering: A. 521–522 (2009) 159–162. https://doi.org/10.1016/j.msea.2008.09.092.

[114] K. Hirata, S. Iikubo, H. Ohtani, First-principles Calculations of the Effects of Mn, Cr, and Ni on Hydrogen Diffusion in BCC, FCC, and HCP Fe, Tetsu-to-Hagane. 105 (2019) 231–239. https://doi.org/10.2355/tetsutohagane.TETSU-2018-070.

[115] B.-H. Chi, T. Nakazawa, K. Shibata, Effects of alloying elements on hardening and restoration behavior of 15Cr-15Ni high hardness non-magnetic stainless steel., ISIJ International. 30 (1990) 615–624. https://doi.org/10.2355/isijinternational.30.615.

[116] C.W. Tien, C.J. Altstetter, Hydrogen-enhanced plasticity of 310S stainless steel, Mater Chem Phys. 35 (1993) 58–63. https://doi.org/10.1016/0254-0584(93)90177-N.

[117] U.F. Kocks, S.R. Chen, On the two distinct effects of thermal activation on plasticity: Application to nickel, Physica Status Solidi (a). 131 (1992) 403–413. https://doi.org/10.1002/pssa.2211310214.

[118] W.A. Curtin, New interpretation of the Haasen plot for solute-strengthened alloys, Scr Mater. 63 (2010) 917–920. https://doi.org/10.1016/j.scriptamat.2010.07.003.

[119] D.M. Barnett, W.C. Oliver, W.D. Nix, The binding force between an edge dislocation and a fermi-dirac solute atmosphere, Acta Metallurgica. 30 (1982) 673–678. https://doi.org/10.1016/0001-6160(82)90116-X.

[120] A.E. Pontini, J.D. Hermida, X-ray diffraction measurement of the stacking fault energy reduction induced by hydrogen in an AISI 304 steel, Scr Mater. 37 (1997) 1831–1837. https://doi.org/10.1016/S1359-6462(97)00332-1.

[121] M.B. Whiteman, A.R. Troiano, The Influence of Hydrogen on the Stacking Fault Energy of an Austenitic Stainless Steel, Physica Status Solidi (b). 7 (1964) K109–K110. https://doi.org/10.1002/pssb.19640070241.

[122] A. Chiba, M. Kim, Suzuki Segregation and Dislocation Locking in Supersaturated Co-Ni-Based Alloy, Mater Trans. 42 (2001) 2112–2116. https://doi.org/10.2320/matertrans.42.2112.

[123] M. Grujicic, X.W. Zhou, W.S. Owen, Monte Carlo analysis of short-range order in nitrogen-strengthened Fe-Ni-Cr-N austenitic alloys, Materials Science and Engineering: A. 169 (1993) 103–110. https://doi.org/10.1016/0921-5093(93)90604-D.

[124] M. Grujicic, W.S. Owen, Models of short-range order in a face-centered cubic Fe-Ni-Cr alloy with a high concentration of nitrogen, Acta Metallurgica et Materialia. 43 (1995) 4201–4211. https://doi.org/10.1016/0956-7151(95)00107-7.

[125] J.C. Fisher, On the strength of solid solution alloys, Acta Metallurgica. 2 (1954) 9–10. https://doi.org/10.1016/0001-6160(54)90087-5.

[126] J. Moriyama, O. Takakuwa, M. Yamaguchi, Y. Ogawa, K. Tsuzaki, Contribution of Cr and Ni to the hydrogen absorption energy in Fe-Cr-Ni austenitic system : A first-principles study, Comput Mater Sci. Submitted (2023).